Advances in Extracting Cloud Composition Information from Spaceborne Infrared Radiances—A Robust Alternative to Brightness Temperatures. Part I: Theory

MICHAEL J. PAVOLONIS

NOAA/NESDIS Center for Satellite Applications and Research, Madison, Wisconsin

(Manuscript received 5 November 2009, in final form 10 May 2010)

ABSTRACT

Infrared measurements can be used to obtain quantitative information on cloud microphysics, including cloud composition (ice, liquid water, ash, dust, etc.), with the advantage that the measurements are independent of solar zenith angle. As such, infrared brightness temperatures (BT) and brightness temperature differences (BTD) have been used extensively in quantitative remote sensing applications for inferring cloud composition. In this study it is shown that BTDs are fundamentally limited and that a more physically based infrared approach can lead to significant increases in sensitivity to cloud microphysics, especially for optically thin clouds. In lieu of BTDs, a derived radiative parameter β, which is directly related to particle size, habit, and composition, is used. Although the concept of effective absorption optical depth ratios β has been around since the mid-1980s, this is the first study to explore the use of β for inferring cloud composition in the total absence of cloud vertical boundary information. The results showed that, even in the absence of cloud vertical boundary information, one could significantly increase the sensitivity to cloud microphysics by converting the measured radiances to effective emissivity and constructing effective absorption optical depth ratios from a pair of spectral emissivities in the 8–12-μm ''window.'' This increase in sensitivity to cloud microphysics is relative to BTDs constructed from the same spectral pairs. In this article, the focus is on describing the physical concepts (which can be applied to narrowband or hyperspectral infrared measurements) used in constructing the β data space.

1. Introduction

The improvement of satellite-based quantitative cloud-top composition (e.g., identification of liquid water, ice, volcanic ash, and dust) determination is important for several reasons. Cloud composition information is critical for understanding the earth radiation budget, water cycle, and atmospheric dynamical/thermodynamical processes. As an example, an accurate estimate of tropical ice cloud coverage is needed to better understand tropical convection, which greatly impacts the large-scale dynamics in the tropics (e.g., Lopez et al. 2009). Skillful identification of optically thin ice clouds (e.g., cirrus) is needed to help to characterize the spatial and temporal coverage of aircraft-produced contrails, which can have long lifetimes (e.g., Minnis et al. 1998) and influence regional climate (Minnis et al. 2004). Quantitative monitoring of airborne terrestrial dust, among other reasons, is important because it plays a role in the complex climate forcing/feedback problem (Evan et al. 2009) and affects tropical storm development (Dunion and Velden 2004).

Cloud composition information can also be used for several practical applications. The identification of volcanic ash clouds is critical for safely directing air traffic (Miller and Casadevall 2000). Furthermore, cloud composition information is useful for studying the temporal evolution of convection. For instance, it can be used to estimate cumulus cloud-top glaciation time and to track anvil growth in an objective and quantitative manner using geostationary satellite data (e.g., Mecikalski and Bedka 2006). Both of these are related to storm strength (e.g., Adler and Fenn 1979). As such, they can potentially be used to make short-term forecasts related to storm severity. This same principle is applicable to tracking the size and shape (e.g., radius) of tropical cyclones, including the semitransparent cirrus outflow. This size and shape information is useful when estimating the strength of cyclones (Olander and Velden 2007). The retrieval of other cloud properties, such as optical depth

Corresponding author address: Michael J. Pavolonis, NOAA/NESDIS Center for Satellite Applications and Research, 1225 W. Dayton St., Madison, WI 53705.
E-mail: mike.pavolonis@noaa.gov

DOI: 10.1175/2010JAMC2433.1

and effective particle size from near-infrared and visible measurements (e.g., Nakajima and King 1990), generally relies on cloud-phase information to constrain the retrieval. Also, as satellite data records continue to grow in size, the importance of data mining increases. Cloud composition information can be used in data-mining applications. For instance, one may want to use data mining to limit a satellite data order to scenes that contain dust over the Atlantic Ocean. This list of applications is in no way exhaustive.

Infrared measurements can be used to obtain quantitative information on cloud microphysics, including cloud composition and particle size, with the advantage that the measurements are independent of solar zenith angle. As such, infrared brightness temperatures (BT) and brightness temperature differences (BTD) have been used extensively in quantitative remote sensing applications for inferring cloud type (e.g., liquid water cloud, ice cloud, dust cloud, volcanic ash cloud, and multilayered cloud) using both threshold and statistical methods (e.g., clustering and machine learning). For instance, Inoue (1985, 1987) used "split window" (11 − 12 μm) brightness temperature differences to identify cloud type. Strabala et al. (1994) and Baum et al. (2000) applied thresholds to 8.5 − 11-μm and 11 − 12-μm BTDs to help to infer cloud phase. Pavolonis and Heidinger (2004) and Pavolonis et al. (2005) used a dynamic thresholding technique to help to infer cloud type, including multilayered cloud, from similar BTDs. Prata (1989), and many others since, have used split-window BTDs to detect volcanic ash and nonvolcanic dust.

All of the aforementioned brightness temperature difference methods have been applied with some success, but it will be shown that, from a spectral point of view, the skill of BT/BTD approaches is fundamentally limited since the measured radiances are sensitive not only to cloud composition but to particle size, particle shape, optical depth, cloud height, surface emissivity, surface temperature, atmospheric gas concentrations, and atmospheric temperature as well. Depending on the situation, the background signal (e.g., surface emissivity, surface temperature, atmospheric temperature, and atmospheric water vapor) can dominate the measured radiance. We will show that more advanced usage of measured infrared radiances can lead to significant increases in sensitivity to cloud microphysics, especially for optically thin clouds. In lieu of BTDs, we use a derived radiative parameter β, which is directly related to particle size, habit, and composition. The subsequent sections of this manuscript will describe the physical basis of our new method for extracting cloud composition information from infrared radiances. In addition, we will motivate the use of certain assumptions in constructing our new data space. In Part II of this study (M. J. Pavolonis 2010, unpublished manuscript, hereinafter Part II), we will use simulations and actual measurements to quantify the gain in skill, relative to BTD-based approaches, that can be expected in determining cloud composition from our new data space. This two-part study does not describe specific algorithms; instead we seek to define a more robust measurement data space from which future, more accurate, algorithms can be developed. To reiterate, Part I of this study is focused on establishing a theoretical foundation for the β data space. In Part II ("proof of concept"), we will show that the theory established in Part I is practically applicable. The term "cloud" will be used when referring to airborne particle distributions of any of the following compositions: liquid water, ice, volcanic ash, or nonvolcanic dust.

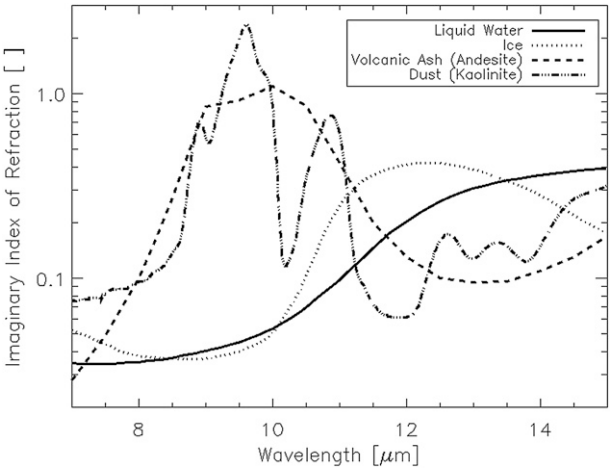

FIG. 1. The imaginary index of refraction for liquid water (solid), ice (dotted), andesite (dashed), and kaolinite (dash–dotted) is shown as a function of wavelength.

2. Physical basis of cloud composition information

The spectral sensitivity to cloud composition is perhaps best understood by examining the imaginary index of refraction m_i as a function of wavelength. The imaginary index of refraction is often directly proportional to absorption/emission strength for a given particle composition in that larger values are indicative of stronger absorption of radiation at a particular wavelength. However, absorption due to photon tunneling, which is proportional to the real index of refraction, can also contribute to the observed spectral absorption under certain circumstances (Mitchell 2000), but for simplicity only absorption by the geometrical cross section, which is captured by the imaginary index of refraction, is discussed here. Figure 1 shows m_i for liquid water (Downing

and Williams 1975), ice (Warren and Brandt 2008), volcanic rock (andesite) (Pollack et al. 1973), and nonvolcanic dust (kaolinite) (Roush et al. 1991). While the exact composition, and hence the m_i, of volcanic ash and dust vary depending on the source, andesite and kaolinite were chosen since both minerals exhibit the often exploited ''reverse absorption'' signature (e.g., Prata 1989). The reverse-absorption signature is responsible for the sometimes-observed negative 11 − 12-μm brightness temperature difference associated with volcanic ash and dust. Furthermore, in this paper, the exact composition assumed for volcanic ash and dust is not critical since we are not attempting to identify specific types of minerals. We are, instead, interested in distinguishing among ice, liquid water, and dust/volcanic ash. Once a dust or volcanic ash cloud is detected, other methods can be used to determine more information about the mineral type (e.g., Pavolonis et al. 2006).

The m_i can be interpreted as follows. In Fig. 1, one sees that around 8.5–10 μm liquid water and ice absorb approximately equally, whereas near 11–13.5 μm ice absorbs more strongly than water. Thus, all else being equal, the difference in measured radiation (or brightness temperature) between an 8.5-μm channel and an 11-μm channel (or 12- or 13.3-μm channel) will be larger for an ice cloud than for a liquid water cloud. The previous statement is only accurate if the liquid water cloud and ice cloud have the same particle concentrations at the same vertical levels in the same atmosphere and have the same particle size and shape distribution. That is what is meant by ''all else being equal.'' Although Fig. 1 is insightful, it can also be deceiving if not interpreted correctly. For example, it is possible that a liquid water cloud in a certain vertical layer with a certain particle distribution will look identical (in measurement space) to an ice cloud at the same vertical layer (in the same atmosphere) but with a different particle distribution. As another example, a scene with a liquid water cloud in one type of atmosphere (e.g., maritime tropical) may exhibit the same measured spectral radiance as a scene with an ice cloud in another type of atmosphere (e.g., continental midlatitude). The same reasoning applies to differentiating between volcanic ash and liquid water/ice or nonvolcanic dust and liquid water/ice.

To increase the sensitivity to cloud composition, the information contained in Fig. 1 must be extracted from the measured radiances as best as possible. One way of doing this is to account for the background conditions (e.g., surface temperature, surface emissivity, atmospheric temperature, and atmospheric water vapor) of a given scene in an effort to isolate the cloud microphysical signal. This is difficult to accomplish with traditional BTs and BTDs. In the following section, we derive a data space that accounts for the background conditions.

3. The beta method

With the assumption of a satellite viewing perspective (e.g., upwelling radiation), a fully cloudy field of view, a nonscattering atmosphere (no molecular scattering), and a negligible contribution from downwelling cloud emission or molecular emission that is reflected by the surface and transmitted to the top of troposphere [Zhang and Menzel (2002) showed that this term is very small at infrared wavelengths], the cloudy radiative transfer equation for a given infrared channel or wavelength can be written as in Eq. (1) (e.g., Heidinger and Pavolonis 2009):

$$R_{\rm obs}(\lambda) = \varepsilon(\lambda)R_{\rm ac}(\lambda) + T_{\rm ac}(\lambda)\varepsilon(\lambda)B(\lambda, T_{\rm eff}) + R_{\rm clr}(\lambda)[1 - \varepsilon(\lambda)]. \quad (1)$$

In Eq. (1), which is derived in appendix A, λ is wavelength, $R_{\rm obs}$ is the observed radiance, $R_{\rm clr}$ is the clear-sky radiance. $R_{\rm ac}$ and $T_{\rm ac}$ are the above-cloud upwelling atmospheric radiance and transmittance, respectively. B is the Planck function, and $T_{\rm eff}$ is the effective cloud temperature. The estimation of the clear-sky radiance and transmittance will be explained later on in this section. The effective cloud emissivity (Cox 1976) is denoted by ε. To avoid using additional symbols, the angular dependence is simply implied. Only fully cloudy fields of view are considered in this manuscript, but in Part II a practical method that is applicable to cloud edges will be presented.

Equation (1) can readily be solved for the effective cloud emissivity as follows:

$$\varepsilon(\lambda) = \frac{R_{\rm obs}(\lambda) - R_{\rm clr}(\lambda)}{[B(\lambda, T_{\rm eff})T_{\rm ac}(\lambda) + R_{\rm ac}(\lambda)] - R_{\rm clr}(\lambda)}. \quad (2)$$

In Eq. (2), the term in brackets in the denominator is the blackbody cloud radiance that is transmitted to the top of the atmosphere (TOA) plus the above-cloud atmospheric radiance. This term is dependent upon the cloud vertical location. This dependence will be discussed in detail in later sections. It is worth noting that a two-layer cloud system, in which the lower cloud layer is assumed to be opaque (e.g., a lower liquid water cloud layer) and the upper layer is allowed to be semitransparent, can easily be accommodated in Eq. (2) if the clear-sky radiance term is replaced with the upwelling TOA radiance from a blackbody cloud layer. Even if the vertical location of the lower cloud layer is chosen based on

climatological values, the estimate of cloud emissivity for the highest cloud layer can be improved for this type of multilayered cloud system. For simplicity, we will only focus on single-layer cloud systems in this paper. Multilayered cloud systems will be addressed in Part II.

The cloud microphysical signature cannot be captured with the effective cloud emissivity alone for a given spectral channel or wavelength. It is the spectral variation of the effective cloud emissivity that holds the cloud microphysical information. To harness this information, the effective cloud emissivity is used to calculate effective absorption optical depth ratios, otherwise known as β ratios (see Inoue 1987; Parol et al. 1991; Giraud et al. 1997; Heidinger and Pavolonis 2009). For a given pair of spectral emissivities [$\varepsilon(\lambda_1)$ and $\varepsilon(\lambda_2)$],

$$\beta_{\text{obs}} = \frac{\ln[1-\varepsilon(\lambda_1)]}{\ln[1-\varepsilon(\lambda_2)]} = \frac{\tau_{\text{abs,eff}}(\lambda_1)}{\tau_{\text{abs,eff}}(\lambda_2)}. \quad (3)$$

Notice that Eq. (3) can simply be interpreted as the ratio of effective absorption optical depth $\tau_{\text{abs,eff}}$ at two different wavelengths. The word ''effective'' is used since the cloud emissivity depends upon the effective cloud temperature. The effective cloud temperature is most often different from the thermodynamic cloud-top temperature since the cloud emission originates from a layer in the cloud. The depth of this layer depends upon the cloud transmission profile, which is generally unknown. One must also consider that the effects of cloud scattering are implicit in the cloud emissivity calculation since the actual observed radiance will be influenced by cloud scattering to some degree. In other words, no attempt is made to separate the effects of absorption and scattering. At wavelengths in the 10–13-μm range, the effects of cloud scattering for upwelling radiation are very small and usually negligible. At infrared wavelengths in the 8–10-μm range, however, the cloud reflectance can make a 1%–3% contribution to the TOA radiance (Turner 2005). Thus, it is best to think of satellite-derived effective cloud emissivity as a radiometric parameter that, in most cases, is proportional to the fraction of radiation incident on the cloud base that is absorbed by the cloud. See Cox (1976) for an in-depth explanation of effective cloud emissivity.

An appealing quality of β_{obs} is that it can be interpreted in terms of the single-scatter properties, which can be computed for a given cloud composition and particle distribution. Following Van de Hulst (1980) and Parol et al. (1991), a spectral ratio of scaled extinction coefficients can be calculated from the single-scatter properties (single-scatter albedo, asymmetry parameter, and extinction cross section), as follows:

$$\beta_{\text{theo}} = \frac{[1.0-\omega(\lambda_1)g(\lambda_1)]\sigma_{\text{ext}}(\lambda_1)}{[1.0-\omega(\lambda_2)g(\lambda_2)]\sigma_{\text{ext}}(\lambda_2)}. \quad (4)$$

In Eq. (4), β_{theo} is the spectral ratio of scaled extinction coefficients, ω is the single-scatter albedo, g is the asymmetry parameter, and σ_{ext} is the extinction cross section. At wavelengths in the 8–15-μm range, where multiple scattering effects are small, β_{theo} captures the essence of the cloudy radiative transfer such that

$$\beta_{\text{obs}} \approx \beta_{\text{theo}}. \quad (5)$$

Eq. (4), which was first shown to be accurate for observation in the 10–12-μm ''window'' by Parol et al. (1991), only depends upon the single-scatter properties. It does not depend upon the observed radiances, cloud height, or cloud optical depth. To illustrate that Eq. (5) is a good approximation in the 8–14-μm range, high-spectral-resolution (0.4-cm^{-1} resolution) radiative transfer simulations were performed using the Line-by-Line Radiative Transfer Model (LBLRTM; Clough and Iacono 1995) to compute spectral gaseous optical depth profiles and a Discrete Ordinate Radiative Transfer (DISORT) method (Stamnes et al. 1988) to account for cloud scattering and absorption. These two radiative transfer tools were combined by Turner (2005) and termed LBLDIS for short. More details concerning LBLDIS can be found in Turner (2005). LBLDIS was used to simulate an ice cloud (composed of plates) in the upper tropical troposphere. The single-scatter properties for this type of cloud were taken from Yang et al. (2005). The cloud optical depth was set to 0.5 at 10 μm (1000 cm^{-1}), and the effective particle radius was varied from 7 to 30 μm. From the simulated radiances, a spectrum of β_{obs} was calculated using Eqs. (2) and (3). The β_{obs} spectrum was constructed such that the wavenumber (or wavelength) in the denominator of Eq. (3) was held constant and the wavenumber in the numerator was varied. An analogous β_{theo} spectrum was calculated using the single-scatter properties as described by Eq. (4). The goal here is to show that Eq. (5) holds true over the 8–14-μm range.

Figure 2 shows the β_{obs} and β_{theo} spectra for various effective particle radii. The results indicate that overall Eq. (5) is a very good approximation, especially at wavelengths of longer than 10 μm. At wavelengths that are shorter than 10 μm, β_{theo} does not fit β_{obs} quite as well. The reasoning for this is as follows. For a given set of cloud microphysics, the amount of scattering will generally increase with decreasing wavelength, which likely imposes a small spectral dependence on the effective cloud temperature across this wavelength range, which was not accounted for here. For simplicity, we will ignore

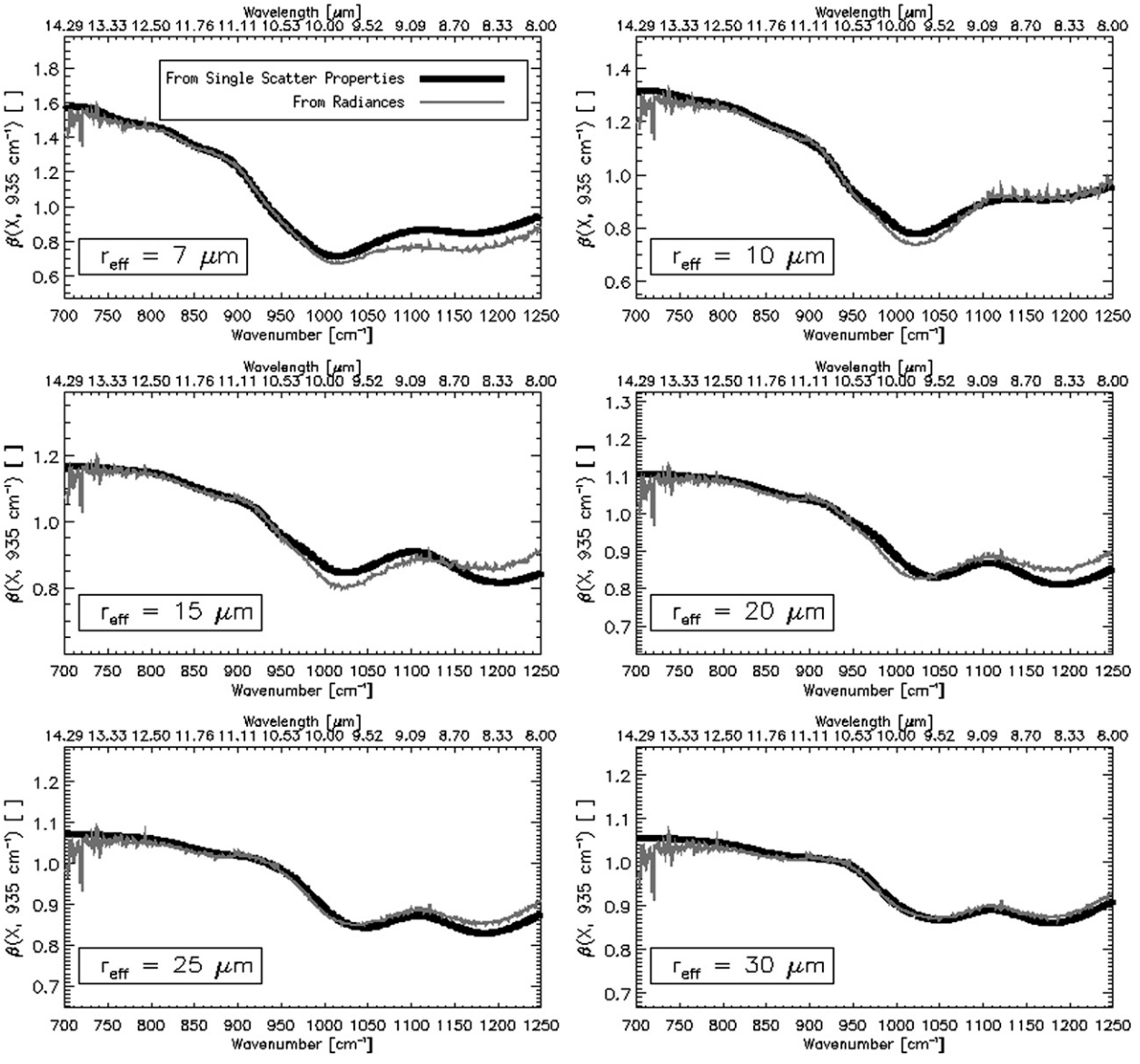

FIG. 2. Spectra of effective absorption optical depth ratios calculated from simulated high-spectral-resolution radiances in the 8–14-μm range are shown in gray (with thinner line style) for an upper-tropospheric ice cloud (composed of plates) with an optical depth of 0.5 at a wavelength of 10 μm. An analogous spectrum of scaled extinction coefficients is also shown in black (with thick line style). Each panel represents a different effective particle radius, as listed in the keys.

this small spectral dependence in T_{eff}. This simplification does not have a large impact on the results presented in this paper, because we are more interested in the relative difference in β as a function of cloud composition, as opposed to the absolute accuracy of Eq. (5).

By using β ratios as opposed to brightness temperature differences, we are not only accounting for the noncloud contribution to the radiances, we are also providing a means to tie the observations back to theoretical size distributions. This framework clearly has practical and theoretical advantages over traditional brightness temperature differences. Parol et al. (1991) first showed that Eq. (5) is a good approximation in the 10–12-μm window. Since that time, faster computers and improvements in the efficiency and accuracy of clear-sky radiative transfer modeling have allowed for more detailed exploration of the β data space and computation of β ratios on a global scale.

a. Cloud composition differences in β space

Since the 8.5 − 11-μm [BTD(8.5 − 11)] and 11 − 12-μm [BTD(11 − 12)] BTDs are often used to determine cloud

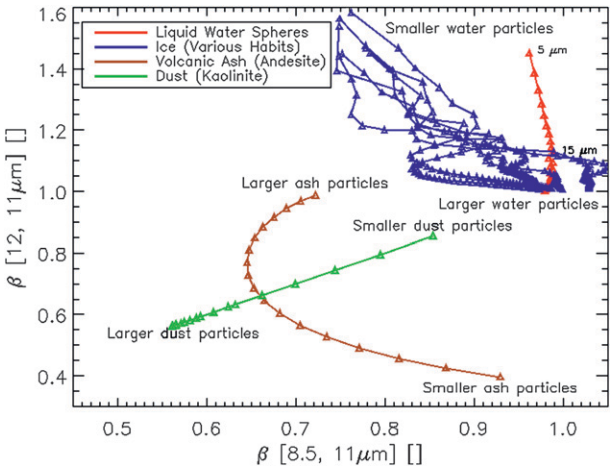

FIG. 3. The 12/11-μm scaled extinction ratio [$\beta(12, 11)$] is shown as a function of the 8.5/11-μm scaled extinction ratio [$\beta(8.5, 11)$] for liquid water spheres (red), various ice crystal habits (blue), andesite spheres (brown), and kaolinite spheres (green). The ice crystal habits shown are plates, aggregates, bullet rosettes, droxtals, hollow columns, solid columns, and spheroids. A range of particle sizes is shown for each composition. For liquid water (ice), the effective particle radius was varied from 5 to 30 (54) μm. The 5- and 15-μm values of liquid water effective radius are labeled. The andesite and kaolinite effective particle radius was varied from 1 to 12 μm. The large and small particle ends of each curve are labeled. The β ratios were derived from the single-scatter properties.

phase (e.g., Strabala et al. 1994; Pavolonis et al. 2005) and to detect volcanic ash and dust (e.g., Pavolonis et al. 2005; Zhang et al. 2006; Prata 1989), these BTDs were selected for analysis. In an analogous way, the β_{theo} for the 8.5-, 11-μm [$\beta(8.5, 11)$] and 11-, 12-μm [$\beta(12, 11)$] wavelengths were analyzed, where the 11-μm emissivity is always placed in the denominator of Eq. (4). Figure 3 shows the relationship between $\beta(8.5, 11)$ and $\beta(12, 11)$ as given by the single-scatter properties [see Eq. (4)] for various cloud compositions with a varying effective particle radius. The effective particle radius is defined as the ratio of the third to second moment of the size distribution (Hansen and Travis 1974). With the exception of ice, all single-scatter properties were calculated using Mie theory. The ice single-scatter properties for seven different habits were taken from the Yang et al. (2005) database. Figure 3 indicates that the sensitivity to particle habit is small relative to the sensitivity to composition and particle size. Thus, variability in β due to ice crystal habit does not inhibit the determination of cloud composition, unless the liquid water effective radius is very large. In addition, one can see that most of the information on cloud thermodynamic phase is given by the difference in absorption between 8.5 and 11 μm, whereas separating meteorological cloud from ash or dust clouds is best performed using a trispectral technique. For ice and liquid water clouds, the difference in absorption at 11 and 12 μm is mostly related to changes in particle size. This figure also indicates that separating dust from ash is difficult to do using just these particular spectral relationships. Unlike BTDs, these β_{theo} relationships are only a function of the cloud microphysical properties.

b. *Estimating the clear-sky radiance and transmittance*

Since the calculation of effective cloud emissivity and hence β_{obs} depends on the clear-sky radiance and transmittance profiles, our mechanism for estimating the clear-sky terms in Eq. (2) is described here. Clear-sky transmittances and radiances are estimated using a fast clear-sky radiative transfer model. These models, which are computationally efficient, will produce a clear-sky transmittance/radiance profile and TOA radiances given an input temperature profile, water vapor profile, ozone profile, surface temperature, surface emissivity, and viewing angle. We currently use a regression-based model (Hannon et al. 1996). The input data (with the exception of viewing angle and surface emissivity) come from numerical weather prediction (NWP) models, such as the National Centers for Environmental Prediction Global Forecast System (GFS). NWP model data are convenient to use because of the constant spatial coverage. Although the current NWP fields often have large errors in some fields, such as the surface temperature over land, they provide needed and useful information. Over the coming years, we expect the NWP fields to improve in accuracy and in spatial resolution, which should act to improve the clear-sky radiance calculations. All of the NWP profile data are interpolated to 101 levels to improve the accuracy of the calculated transmittance profile, especially with regard to absorption channels (e.g., Strow et al. 2003). The spectrally resolved surface emissivity is taken from the global 5-km-spatial-resolution SeeBor database (Seemann et al. 2008). It is important to note that NWP data have been commonly used to drive the clear-sky radiative transfer models used in infrared cloud retrievals. For example, the official Moderate Resolution Imaging Spectroradiometer (MODIS) cloud CO_2-slicing algorithm utilizes this same NWP-based approach to estimate the clear-sky radiance (Menzel et al. 2008).

Since a more complete discussion regarding errors in the TOA clear-sky radiance is given in Heidinger and Pavolonis (2009), only a brief summary is included here. For channels or wavelengths with weighting functions that peak at or near the surface (e.g., window channels), errors in the TOA clear-sky brightness temperatures are generally less than 0.50 K for open ocean. Over land, the GFS surface temperature error exhibits a diurnal cycle in

TABLE 1. Symbols and definitions of the BTD and effective absorption optical depth ratio β_{tropo} Jacobians. The effective absorption optical depth ratio was calculated assuming that the effective cloud temperature is equal to the tropopause temperature. The denominator (numerator) wavelength in the beta ratio is symbolized by $\lambda_D(\lambda_N)$. The BTD is defined as $\lambda_D - \lambda_N$.

BTD Jacobian	β Jacobian	Definition
$\partial \text{BTD}(\lambda_N, \lambda_D)/\partial\beta(\lambda_N, \lambda_D)$	$\partial\beta_{\text{tropo}}(\lambda_N, \lambda_D)/\partial\beta(\lambda_N, \lambda_D)$	The partial derivative with respect to cloud microphysics given by spectral variation in cloud emissivity.
$\partial \text{BTD}(\lambda_N, \lambda_D)/\partial T_{\text{eff}}$	$\partial\beta_{\text{tropo}}(\lambda_N, \lambda_D)/\partial T_{\text{eff}}$	The partial derivative with respect to the effective cloud temperature.
$\partial \text{BTD}(\lambda_N, \lambda_D)/\partial\varepsilon_{\text{cld}}(\lambda_D)$	$\partial\beta_{\text{tropo}}(\lambda_N, \lambda_D)/\partial\varepsilon_{\text{cld}}(\lambda_D)$	The partial derivative with respect to the denominator (λ_D) effective cloud emissivity.
$\partial \text{BTD}(\lambda_N, \lambda_D)/\partial T_{\text{sfc}}$	$\partial\beta_{\text{tropo}}(\lambda_N, \lambda_D)/\partial T_{\text{sfc}}$	The partial derivative with respect to the surface temperature.
$\partial \text{BTD}(\lambda_N, \lambda_D)/\partial T_{\text{atmos}}(\lambda_D)$	$\partial\beta_{\text{tropo}}(\lambda_N, \lambda_D)/\partial T_{\text{atmos}}(\lambda_D)$	The partial derivative with respect to the denominator (λ_D) clear-sky atmospheric transmittance.
$\partial \text{BTD}(\lambda_N, \lambda_D)/\partial\beta_{\text{atmos}}(\lambda_N, \lambda_D)$	$\partial\beta_{\text{tropo}}(\lambda_N, \lambda_D)/\partial\beta_{\text{atmos}}(\lambda_N, \lambda_D)$	The partial derivative with respect to the spectral variation of clear-sky atmospheric transmittance.
$\partial \text{BTD}(\lambda_N, \lambda_D)/\partial\varepsilon_{\text{sfc}}(\lambda_D)$	$\partial\beta_{\text{tropo}}(\lambda_N, \lambda_D)/\partial\varepsilon_{\text{sfc}}(\lambda_D)$	The partial derivative with respect to the denominator (λ_D) surface emissivity.
$\partial \text{BTD}(\lambda_N, \lambda_D)/\partial\beta_{\text{sfc}}(\lambda_N, \lambda_D)$	$\partial\beta_{\text{tropo}}(\lambda_N, \lambda_D)/\partial\beta_{\text{sfc}}(\lambda_N, \lambda_D)$	The partial derivative with respect to the spectral variation of surface emissivity.

which the surface temperature is significantly underestimated during the day and slightly overestimated at night. Given the large uncertainties in surface temperature and uncertainties in surface emissivity, the TOA clear-sky radiance calculation over land is prone to fairly large errors (up to 15 K over desert surfaces around local solar noon), although the impact of these errors is not always severe, depending on the cloud optical depth. In Part II, it will be shown that cloud composition information inferred using the β method is not significantly coupled to the NWP model and that fairly large errors in the clear-sky radiance can be tolerated. Thus, assimilation of cloud composition information, extracted using the β method, into numerical models should not be prohibitive. Last, it is important to note that the specific radiative transfer model and ancillary data (e.g., NWP, surface observations, independent remote sensing data, and rawinsondes) used to generate the clear-sky radiances and transmittances do not significantly affect the results shown in this paper, as long as the estimates are reasonable. The physical concepts are not at all dependent on the clear-sky radiative transfer scheme chosen.

4. Sensitivity of beta to cloud vertical structure

As shown earlier, the cloud emissivity is dependent on the vertical distribution of cloud particles between the upper and lower vertical boundaries. In the absence of high-quality independent cloud vertical boundary information, such as from a lidar, the effective cloud temperature T_{eff} is considered to be unknown. Previous studies have shown that infrared window channels are mostly insensitive to the T_{eff} for semitransparent clouds (e.g., Heidinger and Pavolonis 2009). Given this information, can one assume a constant T_{eff} and still effectively isolate the cloud microphysical signal using window channels? To be more specific, since most clouds are at or below the tropopause, can we assume that $T_{\text{eff}} = T_{\text{tropo}}$?

To answer this question, we derived analytical expressions for various BTD and β_{tropo} Jacobians, where β_{tropo} is the β calculated using Eqs. (2) and (3) assuming that $T_{\text{eff}} = T_{\text{tropo}}$. The purpose of this analysis is to determine the sensitivity of a given BTD and β_{tropo} to cloud microphysics (given by the true β taken from single-scatter properties), the effective cloud temperature, the effective cloud emissivity, the surface temperature, the surface emissivity, and the atmospheric gaseous transmittance. The complete list of partial derivatives (Jacobians) is shown in Table 1. All of the analytical expressions, which are listed in appendix B, were derived using Eqs. (1)–(3) and the Planck function.

GFS data were used to evaluate these analytical expressions for a variety of scenes. A description of the GFS can be found in Hamill et al. (2006). We chose to simulate the 8.5-, 11-, and 12-μm channels on the Spinning Enhanced Visible and Infrared Imager (SEVIRI). SEVIRI, which is in geostationary orbit, is a 12-channel imaging instrument with a spatial resolution of 3 km at nadir for the infrared channels. (For more information on SEVIRI, see http://www.eumetsat.int/). We chose to simulate SEVIRI radiances primarily out of convenience since we are using it for other studies. The conclusions drawn from these analyses do not change if channels with a similar central wavelength from another sensor are simulated. For reasons described in section 3a, the 8.5 − 11- and 11 − 12-μm BTDs and the β_{tropo} for the 8.5-, 11-μm and 11-, 12-μm channel pairs were analyzed, where the 11-μm channel emissivity is always placed in the denominator of Eq. (3). From here forward the BTDs and β_{tropo} are referred to as

BTD(8.5 − 11), BTD(11 − 12), $\beta_{\text{tropo}}(8.5, 11)$, and $\beta_{\text{tropo}}(12, 11)$, respectively.

Figure 4 shows the GFS 12-h forecast of surface temperature (Fig. 4a) and total precipitable water (Fig. 4b) over a spatial domain consistent with a SEVIRI full disk for an arbitrarily chosen time (forecast valid at 1345 UTC 2 August 2006). The August monthly-mean 8.5- and 11-μm surface emissivities from the SeeBor database are also shown in Figs. 4c,d. The Jacobians were evaluated for several different locations in this spatial domain. Excluding bare land surfaces, the results vary only slightly. Thus, Jacobians for a maritime tropical location and a location in the Sahara Desert, denoted by the triangles on Fig. 4, are shown here. For each scene, the 11-μm cloud emissivity was varied from 0.01 to 0.99 and the location of the cloud in the vertical direction and the cloud composition were varied. The location of the cloud in the vertical direction was specified using a tropopause-following pressure coordinate analogous to the terrain-following sigma coordinates commonly employed by NWP models. A tropopause-following coordinate system was chosen to account for the spatial variability of the tropopause height. The goal is to put the cloud in a vertical location such that the mass of air between the cloud top and the tropopause is roughly constant regardless of the height of the tropopause. The cloud pressure level is determined using the following expression:

$$P_{\text{eff}} = (P_{\text{tropo}} - P_{\text{sfc}})\sigma + P_{\text{sfc}}. \quad (6)$$

In Eq. (6), P_{eff} is the cloud pressure used to determine the effective cloud temperature by matching P_{eff} to the corresponding temperature in the model profiles, P_{tropo} is the pressure of the thermodynamically defined model tropopause, P_{sfc} is the surface pressure, and σ is the weighting factor that determines the vertical location of the cloud. In these sensitivity studies three different weighting factors ($\sigma = 0.87, \sigma = 0.63$, and $\sigma = 0.33$) were used. The 0.87 weighting factor results in a cloud located in the upper troposphere, which is about 75–120 hPa (~3–5 km) lower than the tropopause pressure. This is important since we are assuming a T_{eff} consistent with the tropopause and we want to make sure that the true T_{eff} is significantly different than the one we assumed. The 0.63 and 0.33 weighting factors are consistent with the middle and lower troposphere, respectively.

Three different cloud compositions—ice, liquid water, and andesite (volcanic ash)—were simulated. For ice, a true β value consistent with a plate habit and an effective particle radius of 20 μm, based on the single-scatter database of Yang et al. (2005), were used. The true β values for liquid water and volcanic ash were based upon single-scatter properties generated using Mie theory assuming spherical particles. A β value consistent with an effective radius of 10 μm was chosen for liquid water. For volcanic ash, a β value consistent with an effective radius of 2 μm was chosen. All parameters used in these simulations are summarized in Table 2.

For simplicity, only single-layer clouds are considered in this analysis, even though both the BTD and β_{tropo} will be sensitive to multiple cloud layers when the highest cloud layer is semitransparent. In Part II, real measurements will be used to assess the impact of multilayered clouds on both the BTD and β_{tropo}. Partial cloudiness will also be addressed in Part II of this study. The goal here is to provide theoretical insight into the sensitivity of the BTD and β_{tropo} to cloud microphysics relative to other variables under straightforward conditions.

In this analysis, all of the Jacobians were arbitrarily scaled to a 1% change (relative to the current value) in the independent variables to obtain consistent units for a given set of BTD or β_{tropo} partial derivatives. This sort of scaling allows us to answer the following question. If each independent variable is perturbed by the same arbitrarily chosen amount, relative to the current value, while holding every other variable constant, which perturbation causes the greatest change in BTD or β_{tropo}?

a. Maritime tropical scene

Sensitivity results for the 8.5-, 11-μm and the 11-, 12-μm channel combinations are shown for the maritime tropical scene in Figs. 5 and 6, respectively. The scaled β_{tropo} Jacobians are displayed on the left-hand side, and the scaled BTD Jacobians are on the right-hand side. The top (middle; bottom) row in these multipanel figures shows the sensitivity to the ice (volcanic ash; liquid water) cloud at the $\sigma = 0.87$ ($\sigma = 0.63$; $\sigma = 0.33$) level. Because of the aforementioned scaling, the magnitude of a given Jacobian is arbitrary; thus it is the relative difference in magnitude between the Jacobians within each separate panel of the figure that is significant. As such, the magnitude of each scaled Jacobian was normalized by the magnitude of the cloud microphysics Jacobian, where blue (red) colors indicate that the magnitude of the Jacobian was less (greater) than the magnitude of the cloud microphysics Jacobian.

With regard to the ice cloud, which is located in the upper troposphere, about 4 km below the tropopause, β_{tropo} is most sensitive to the cloud microphysics when the cloud emissivity is less than about 0.80–0.87, depending on which spectral channels are considered. As expected, at larger emissivities, β_{tropo} gradually becomes most sensitive to the effective cloud temperature and the cloud emissivity. In contrast, the BTD for the 8.5-, 11-μm pair is never most sensitive to cloud microphysics, and the BTD for the 11-, 12-μm pair is only most

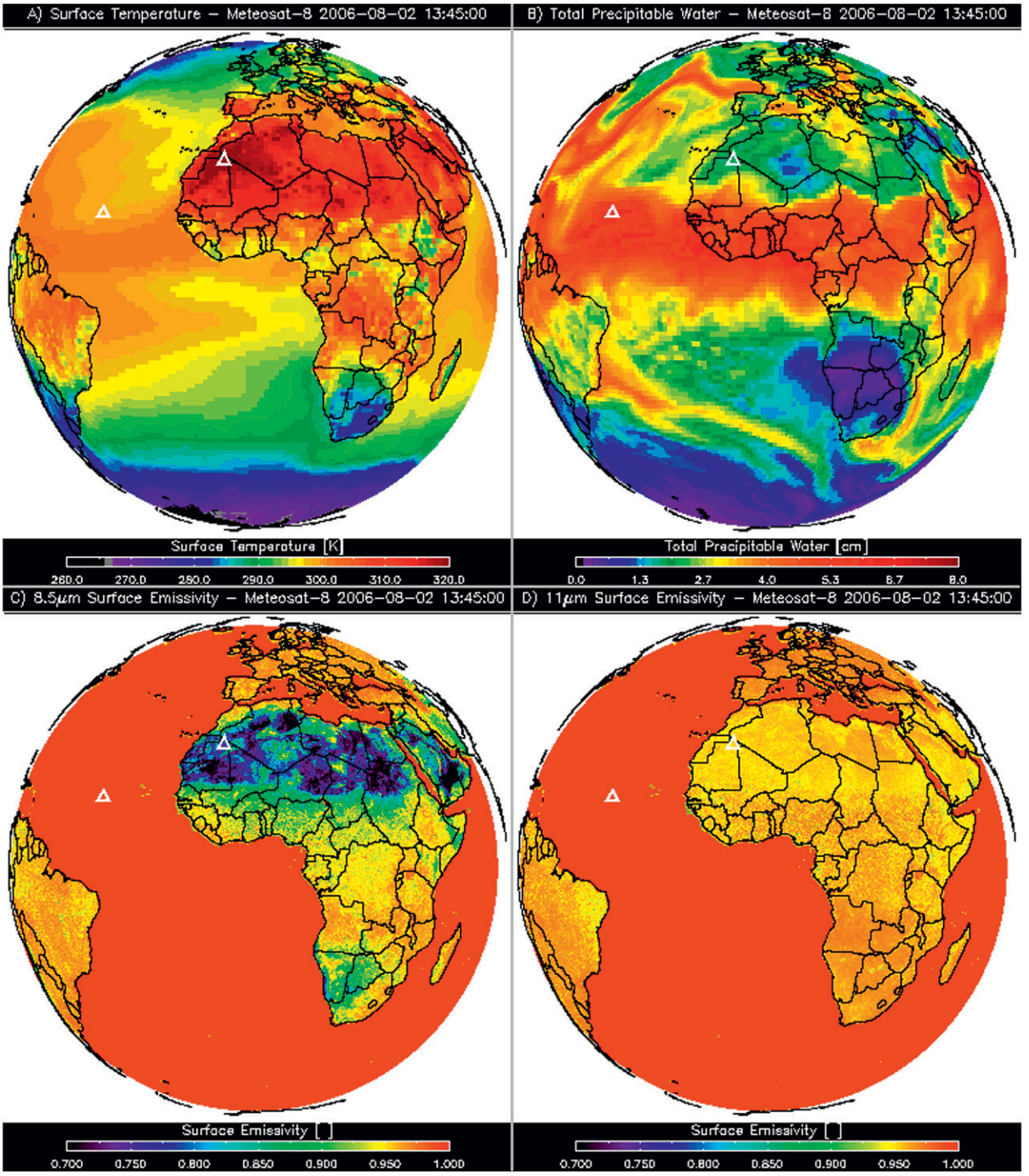

FIG. 4. (a) Surface temperature (K), (b) total precipitable water (cm), (c) 8.5-μm surface emissivity, and (d) 11-μm surface emissivity are shown mapped to a full disk viewed by a geostationary radiometer. The surface temperature and precipitable water are taken from a 12-h GFS forecast valid at 1345 UTC 2 Aug 2006. The surface emissivity is a monthly mean taken from the SeeBor database. The white triangles indicate locations at which Jacobians of the infrared radiative transfer equation were evaluated using these and other inputs from the GFS.

TABLE 2. A description of the parameters used in various radiative transfer model simulations of a maritime tropical and Sahara Desert scene.

Parameter	Maritime tropical	Sahara Desert
Surface temperature	299 K	321.94 K
8.5-μm surface emissivity	0.990	0.738
11-μm surface emissivity	0.990	0.953
12-μm surface emissivity	0.990	0.978
Total precipitable water	6.24 cm	1.85 cm
8.5-μm clear atmospheric transmittance	0.433	0.784
11-μm clear atmospheric transmittance	0.353	0.870
12-μm clear atmospheric transmittance	0.209	0.800
Ice/ash/liquid water cloud σ	0.87/0.63/0.33	0.87/0.63/0.33
Ice/ash/liquid water cloud effective height	11.78/6.87/3.00 km	12.01/7.26/3.49 km
Ice/ash/liquid water cloud effective pressure	221.46/440.12/713.45 hPa	214.88/421.39/679.52 hPa
Ice/ash/liquid water cloud effective temperature	224.66/261.99/282.79 K	224.93/254.55/286.43 K
Ice/ash/liquid water cloud β(8.5, 11 μm)	0.836/0.705/0.981	0.836/0.705/0.981
Ice/ash/liquid water cloud β(12, 11 μm)	1.07/0.564/1.21	1.07/0.564/1.21
Ice/ash/liquid water cloud effective radius	20/2/10 μm	20/2/10 μm

sensitive to cloud microphysics at large emissivities. Note how the BTDs are very sensitive to surface temperature over most of the range of emissivities while the sensitivity of β_{tropo} to noncloud variables is very small. Although not shown, these general conclusions for an upper-tropospheric cloud hold when other cloud compositions or ice crystal habits are considered.

The volcanic ash cloud at the $\sigma = 0.63$ level, which is about 9 km below the tropopause, exhibits a reduced sensitivity to cloud microphysics relative to the ice cloud at the $\sigma = 0.87$ level. Similar to the upper-tropospheric ice cloud, β_{tropo} is considerably more sensitive to cloud microphysics than are the BTDs. The β_{tropo} Jacobians indicate a slightly stronger sensitivity to noncloud variables, especially the surface temperature. This is because of the larger difference between the assumed vertical cloud location and the true cloud location.

The liquid water cloud was placed about 13 km below the tropopause, in the lower troposphere at $\sigma = 0.33$. In this case, a very large error in the cloud vertical location resulted from our top-of-troposphere assumption, and, as such, β_{tropo} is most sensitive to the effective cloud temperature and not to cloud microphysics. Results in Part II will show that this enhanced sensitivity to T_{eff} generally does not adversely impact the ability of β_{tropo} to differentiate liquid water and ice clouds with improved skill relative to the BTDs. Despite this large error in the vertical cloud location, β_{tropo} is still noticeably more sensitive to cloud microphysics than the corresponding BTDs.

b. Sahara Desert scene

Bare land surfaces such as those found in the Sahara Desert are characterized by lower infrared emissivities (relative to most other surfaces) with a large spectral variation in the 8.5–12-μm window. Because of these features in the surface emissivity, it is well known that BTDs associated with semitransparent clouds can be dominated by these surface signals (e.g., Pavolonis et al. 2005). Figures 7 and 8 show that this is, in fact, the case for the 8.5-, 11-μm and the 11-, 12-μm channel pairs, respectively. The BTD(8.5 − 11) (Fig. 7) is very sensitive to surface emissivity over most of the range of cloud emissivities for each cloud type considered. Conversely, β_{tropo}(8.5, 11) is very sensitive to cloud microphysics for midlevel and high clouds over a large range of cloud emissivities. The β_{tropo}(8.5, 11) sensitivity results for the low liquid water cloud indicate that an accurate estimation of the cloud height is needed over low-emissivity surfaces to better isolate the cloud microphysical signal. This is likely due to the reduced difference between the upwelling clear-sky radiance and the cloudy-sky radiance caused by the reduced surface emissivities. The BTD(8.5 − 11) is also very insensitive to cloud microphysics under these same conditions. The difference in surface emissivity between the 11- and 12-μm channels is not quite as large as for the 8.5- and 11-μm channels, and the magnitude of the 12-μm surface emissivity is larger than the 8.5-μm surface emissivity. Thus, the β_{tropo}(12, 11) for the midlevel ash cloud and the low-level liquid water cloud exhibits a much greater sensitivity to cloud microphysics than does the β_{tropo}(8.5, 11) under the same conditions. Overall, β_{tropo}(12, 11) is much more sensitive to cloud microphysics than is BTD(11 − 12).

c. Alternative cloud vertical structure assumptions

The results in the previous section indicate that the assumption of $T_{\text{eff}} = T_{\text{tropo}}$ used in constructing β_{tropo} from combinations of the 8.5-, 11-, and 12-μm channels is very effective, but is it possible to improve upon this

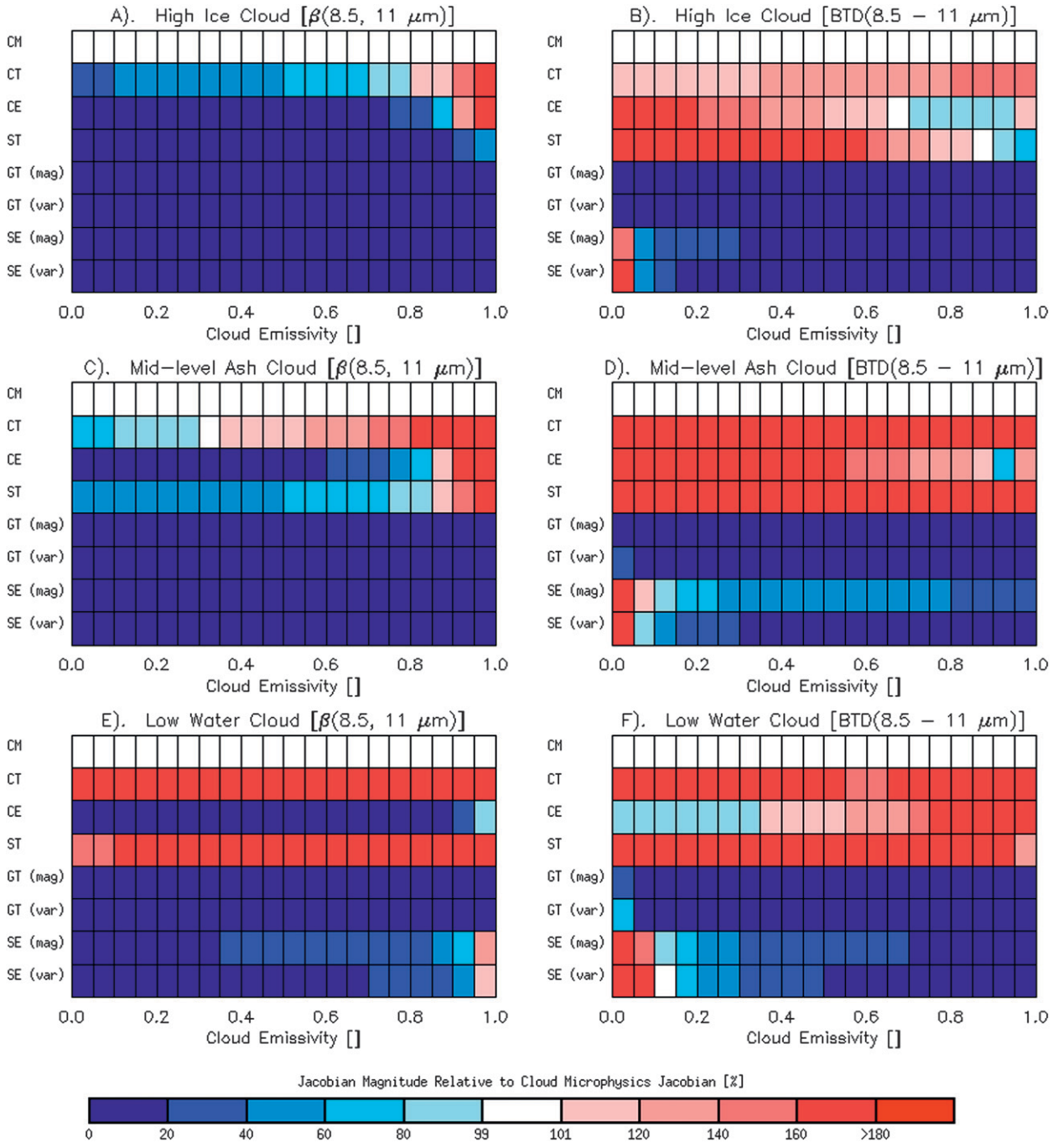

FIG. 5. Evaluation of (right) 8.5 − 11-μm brightness temperature difference Jacobians and (left) 8.5/11-μm effective absorption optical depth ratio Jacobians, calculated assuming an effective cloud temperature equal to the tropopause temperature, for a maritime tropical location. For each dependent variable, the partial derivative with respect to cloud microphysics (CM), cloud effective temperature (CT), 11-μm cloud emissivity (CE), surface temperature (ST), total 11-μm clear-sky atmospheric transmittance [GT (mag)], the spectral variation of the clear-sky atmospheric transmittance [GT (var)], the 11-μm surface emissivity [SE (mag)], and the spectral variation of the surface emissivity [SE (var)] were evaluated as a function of the 11-μm cloud emissivity. All Jacobians were scaled to a 1% change in the dependent variable and then normalized by the respective CM Jacobian. Blue (red) colors indicate that the magnitude of the Jacobian is less (greater) than the magnitude of the CM Jacobian. Three different types of clouds were considered: (a),(b) an ice cloud in the upper troposphere (but significantly lower than the tropopause), (c),(d) a volcanic ash cloud in the middle troposphere, and a (e),(f) liquid water cloud in the lower troposphere.

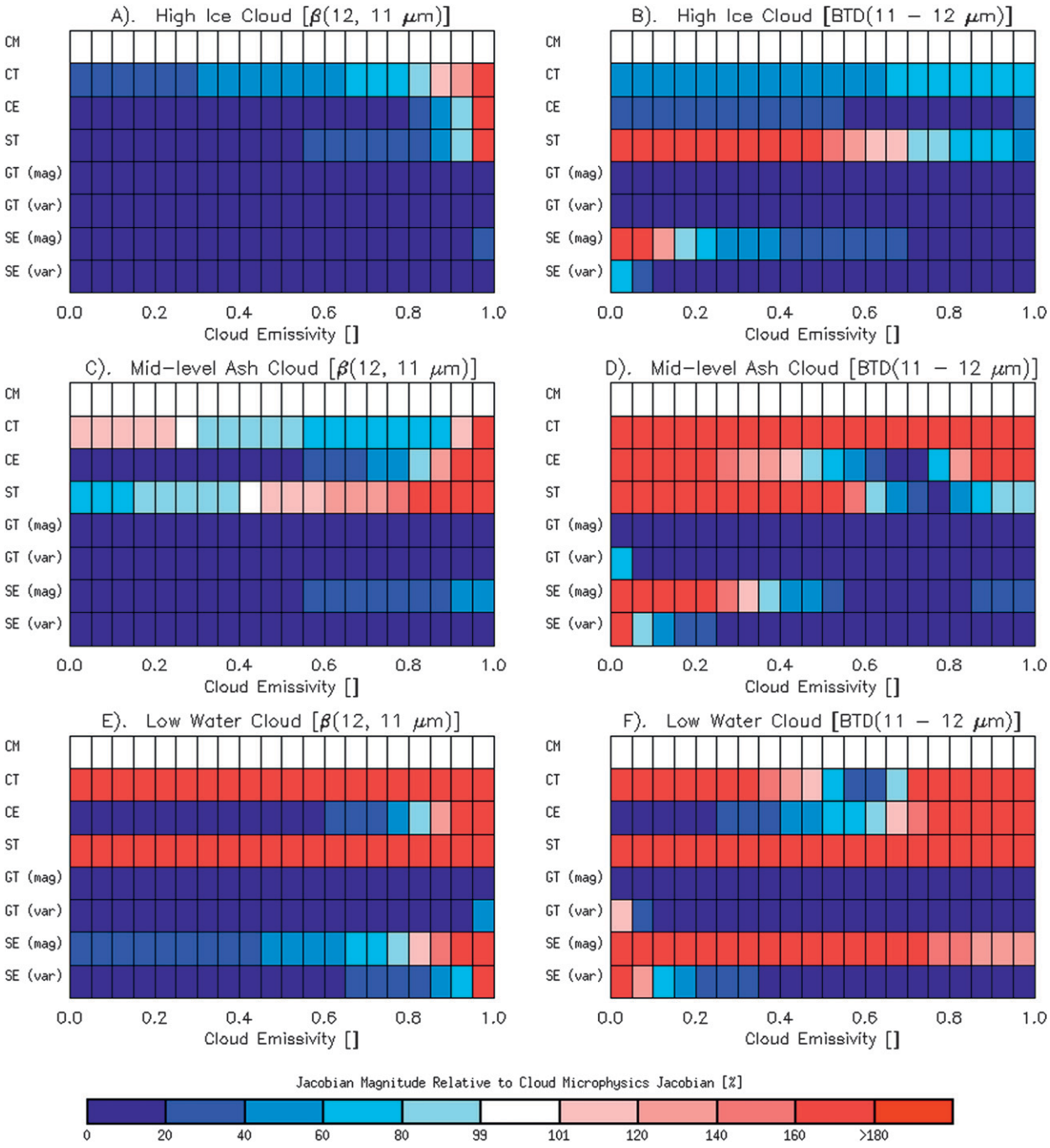

FIG. 6. As in Fig. 5, except that the 11 − 12-μm brightness temperature difference and the 12/11-μm effective absorption optical depth ratio were considered.

assumption under certain conditions? To be more specific, can the microphysical sensitivity for mid- and lower-level clouds be improved if one has some a priori knowledge regarding the approximate cloud emissivity? One method for determining whether a cloud has a large cloud emissivity ($\varepsilon > 0.90$) is to calculate β_{obs} for a given channel pair choosing a cloud vertical level such that the 11-μm emissivity is equal to 0.990. A value of 0.990 allows the other emissivity in the channel pair to have values greater than the 11-μm emissivity yet smaller than 1.0. In other words, using the 11-μm channel as the first channel used in calculating β, the cloud emissivity of

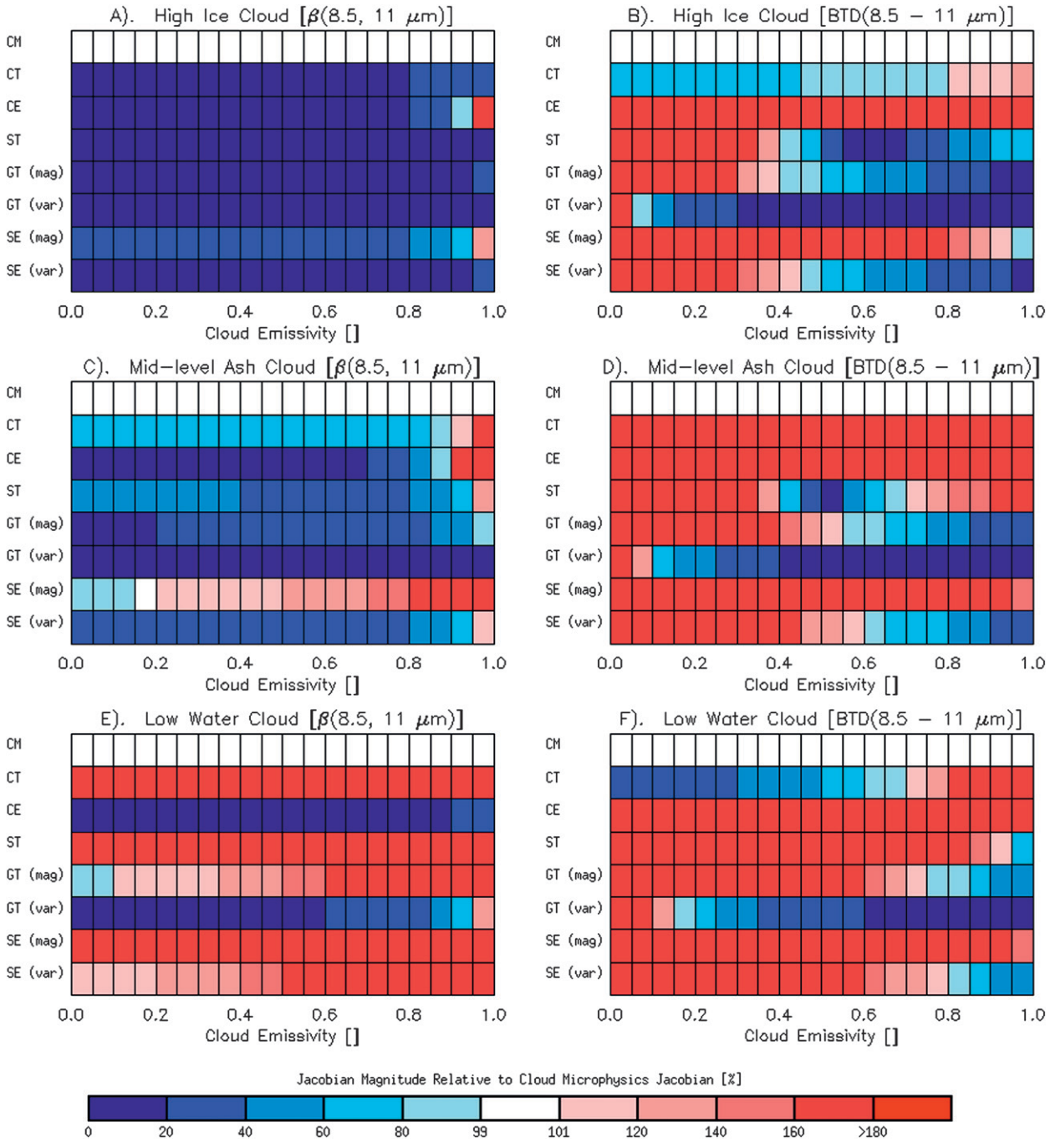

FIG. 7. As in Fig. 5, except that the Jacobians were evaluated for a scene located over the Sahara Desert.

the second channel is determined using the vertical level that gives an 11-μm cloud emissivity of 0.990. If the cloud actually has a large 11-μm emissivity, then the β calculated using this assumption should fall well within the expected theoretical range given by the single-scatter properties. If the cloud has an 11-μm emissivity much smaller than 0.990, the β_{obs} should be greatly influenced by the spectral variability in surface emissivity and clear-sky gaseous transmittance and thus may not fall within the expected theoretical range. The following analysis illustrates this point.

Figures 9 and 10 show the $\beta(12, 11)$ and $\beta(8.5, 11)$ calculated under the assumption that 11-μm cloud emissivity must be equal to 0.990 when the actual 11-μm cloud

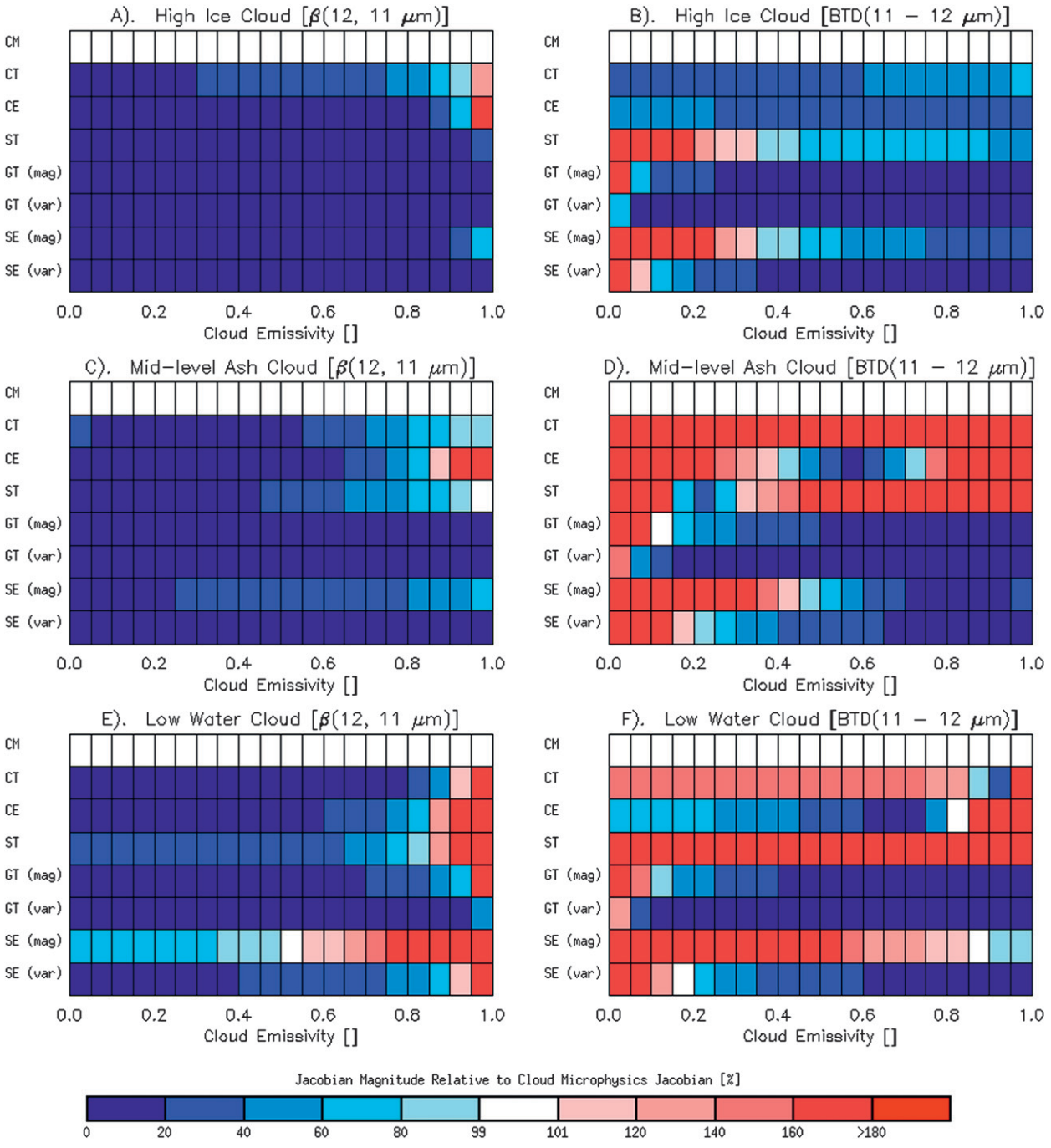

FIG. 8. As in Fig. 7, except that the 11 − 12-μm brightness temperature difference and the 12/11-μm effective absorption optical depth ratio were considered.

emissivities were varied from 0.01 to 0.999. An ice cloud at the $\sigma = 0.87$ level and a liquid water cloud at the $\sigma = 0.33$ level were considered. The same maritime tropical (Fig. 9) and Sahara Desert (Fig. 10) conditions used in the Jacobian analysis presented in the previous sections were applied to generate these figures. The relevant parameters used in this analysis are shown in Table 2. The expected ranges of $\beta(12, 11)$ and $\beta(8.5, 11)$, which are given by the single-scatter-property-derived betas shown in Fig. 3, are denoted by the dotted line in Figs. 9 and 10.

Under the maritime tropical conditions listed in Table 2, $\beta(12, 11)$ is a very good indicator of whether a cloud has

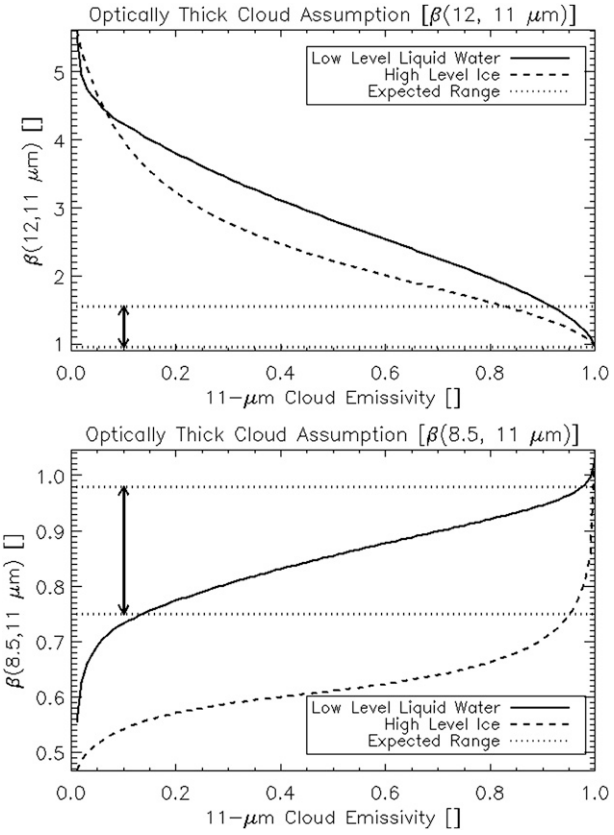

FIG. 9. Calculations showing the (top) 12/11-μm and (bottom) 8.5/11-μm effective absorption optical depth ratio β derived by assuming a cloud vertical level that gives an 11-μm cloud emissivity equal to 0.99 (performed regardless of the true cloud emissivity). Each β is expressed as a function of the true 11-μm cloud emissivity for an upper-tropospheric ice cloud (dashed line) and a lower-tropospheric liquid water cloud (solid line). The range of values expected based on the single-scatter properties is given by the dotted line. These calculations were performed for a maritime tropical location.

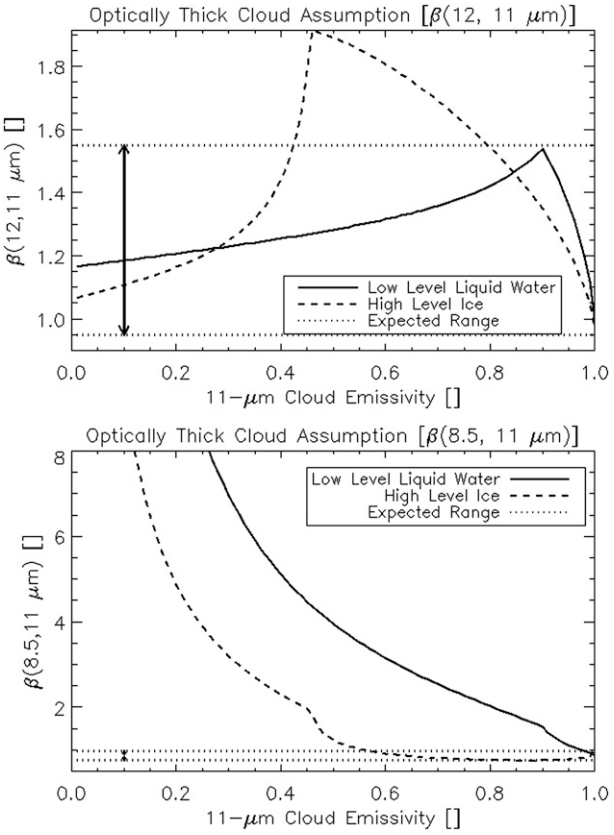

FIG. 10. As in Fig. 9, except that a location over the Sahara Desert was considered.

an 11-μm emissivity >0.90 because unphysical values of $\beta(12, 11)$ are found over the low and middle ranges of 11-μm cloud emissivity. It is important to note that we are not attempting to retrieve the actual cloud emissivity; instead we are looking for a quick and effective way to determine which rough emissivity range (e.g., semitransparent or near opaque) the cloud falls into. The $\beta(12, 11)$ owes its sensitivity to cloud opacity to the difference in atmospheric weighting functions between the two channels. Conversely, $\beta(8.5, 11)$ is not a very strong indicator of relative cloud opacity in this case because the difference in the 8.5- and 11-μm clear-sky atmospheric optical depth (0.84 and 1.04, respectively) is small relative to the difference in the 11- and 12-μm clear-sky optical depth (1.04 and 1.57, respectively). Differences in atmospheric optical depth are important, especially since the surface emissivity is spectrally constant in this case. The clear-sky atmospheric optical depth (or alternatively, the atmospheric transmittance) affects the difference between the black cloud radiance, $B(\lambda, T_{\text{eff}})T_{\text{ac}}(\lambda) + R_{\text{ac}}(\lambda)$ in Eq. (2), and the clear-sky radiance $R_{\text{clr}}(\lambda)$. In other words, the upwelling TOA radiance from an elevated (e.g., above the surface) blackbody surface, and the atmosphere above $[B(\lambda, T_{\text{eff}})T_{\text{ac}}(\lambda) + R_{\text{ac}}(\lambda)]$, converges to the clear-sky radiance $[R_{\text{clr}}(\lambda)]$ at a higher (colder in this case) atmospheric level for wavelengths that have a higher peaking atmospheric weighting function (or a surface emissivity that is significantly less than 1.0). The black cloud radiance is the only term in Eq. (2) that is altered when a new cloud vertical level is considered. The maritime tropical results hold for most other conditions, but there are exceptions, as described below.

When the surface emissivity exhibits large spectral variations, such as over the Sahara Desert, the maritime tropical results are no longer valid. Figure 10 shows that $\beta(8.5, 11)$ can be used to identify the presence of opaque liquid water clouds over surfaces that have a small 8.5-μm surface emissivity (0.738 in this case) relative to the 11-μm

surface emissivity (0.953 in this case). The smaller surface emissivity at 8.5 μm leads to a much smaller difference between the 8.5-μm black cloud radiance and the 8.5-μm clear-sky radiance in the denominator of Eq. (2) relative to the same difference at 11 μm. The $\beta(12, 11)$ exhibits less sensitivity over the Sahara Desert for two reasons. The 11- and 12-μm weighting functions differ less since the air mass is very dry. However, more important, the 12-μm surface emissivity (0.978) is greater than the 11-μm surface emissivity (0.953), which acts to reduce the impact of the spectral variation in clear-sky atmospheric transmittance. Overall, these results indicate that it is possible to identify optically thick clouds using β. Given a priori knowledge of an opaque/near-opaque cloud, it may be possible to improve upon the $T_{\text{eff}} = T_{\text{tropo}}$ assumption by taking T_{eff} to be consistent with an optically thick cloud.

5. Conclusions

Although the concept of effective absorption optical depth ratios β has been around since at least the mid-1980s, this is the first study to explore the use of β for inferring cloud composition (ice, liquid water, ash, dust, etc.) in the absence of cloud vertical boundary information. The results showed that, even in the absence of cloud vertical boundary information, one could significantly increase the sensitivity to cloud microphysics by converting the measured radiances to effective emissivity and constructing effective absorption optical depth ratios from a pair of spectral emissivities. The spectral pair(s) can be chosen to take advantage of differences in the spectral absorption for different compositions. The increase in sensitivity to cloud microphysics is relative to brightness temperature differences (BTDs) constructed from the same spectral pairs.

BTDs have traditionally been used to infer cloud composition. A detailed sensitivity analysis indicated that, for clouds with an 11-μm emissivity of less than about 0.85, commonly used BTDs constructed from 8.5-, 11-, and 12-μm brightness temperatures are more sensitive to noncloud variables—such as surface temperature, surface emissivity, and clear-sky atmospheric transmittance—than to cloud microphysics (which includes cloud composition). In contrast, β constructed from the same spectral radiances showed a much greater sensitivity to cloud microphysics, despite the fact that a constant, and inaccurate, cloud level (taken to be the top of the troposphere) was assumed when calculating cloud emissivity. This result occurs because the spectral variation in radiance in the infrared window is largely insensitive to the cloud effective temperature. Additional analysis indicated that β could also be used to identify clouds that are optically thick (cloud emissivity >0.9). This knowledge can potentially be used to improve the sensitivity to cloud microphysics, and hence composition, for those same optically thick clouds. Another advantage of using β as opposed to BTDs is that β can be directly related to theoretical cloud particle distributions via the single-scatter properties.

While the physical concepts described in this manuscript apply to broadband and high-spectral-resolution (hyperspectral) infrared measurements, hyperspectral measurements offer a few clear advantages. Hyperspectral measurements provide more complete spectral coverage (i.e., there are generally fewer spectral gaps) and, hence, are a better source of microphysical information. The microphysical information is more robust because more of the detail contained in the index-of-refraction spectra can be resolved. The increased spectral sampling of hyperspectral measurements also allows one to smooth out noise associated with the measurements and/or the clear-sky calculations.

The goal of this manuscript was to describe the physical basis of a new method for extracting cloud composition information from infrared radiances and to motivate the use of certain assumptions in constructing our new β-based data space. In a companion paper (Part II), we will use simulations and actual measurements to quantify the gain in skill, relative to BTD-based approaches, that can be expected in determining cloud composition from our new data space. The results in Part II will show that the gain in skill is consistent with the theoretical basis established in this study.

Acknowledgments. This paper is dedicated to the late Mr. Hal Woolf of UW-CIMSS, who provided the fast clear-sky radiative transfer model. Dr. Dave Turner (University of Wisconsin) provided the LBLDIS radiative transfer model. We thank Drs. Andrew Heidinger and Bryan Baum for their very significant reviews of this manuscript and subsequent discussions. We also thank the three anonymous reviewers for their valuable comments and suggestions. The views, opinions, and findings contained in this report are those of the author(s) and should not be construed as an official National Oceanic and Atmospheric Administration or U.S. government position, policy, or decision.

APPENDIX A

Derivation of the All-Sky Infrared Radiative Transfer Equation

For upwelling infrared radiation, the surface reflectance term is generally very small (Zhang and Menzel

2002) and molecular scattering is negligible, and therefore the TOA clear-sky radiance $R_{clr}(\lambda)$ can be expressed as

$$R_{clr}(\lambda) = \varepsilon_{sfc}(\lambda)B(\lambda, T_{sfc})T_{atmos}(\lambda) + R_{atmos}(\lambda). \quad \text{(A1)}$$

In Eq. (A1), λ is the wavelength, $\varepsilon_{sfc}(\lambda)$ is the surface emissivity, B is the Planck function, T_{sfc} is the surface temperature, $T_{atmos}(\lambda)$ is the surface-to-TOA transmittance, and $R_{atmos}(\lambda)$ is the integrated atmospheric radiance that is transmitted to the TOA. Equation (A1) can be rewritten as

$$R_{clr}(\lambda) = \varepsilon_{sfc}(\lambda)B(\lambda, T_{sfc})T_{bc}(\lambda)T_{ac}(\lambda) + R_{bc}(\lambda)T_{ac}(\lambda) + R_{ac}(\lambda). \quad \text{(A2)}$$

In Eq. (A2) the total column upwelling atmospheric transmittance T_{atmos} and radiance R_{atmos} terms are simply decomposed into "below cloud (bc)" and "above cloud" layers, which will aid in the simplification of the cloudy infrared radiative transfer equation.

With the assumption of a fully cloudy field of view, a nonscattering atmosphere (no molecular scattering), and a negligible contribution from downwelling cloud emission or molecular emission that is reflected by the surface and transmitted to the top of troposphere [Zhang and Menzel (2002) showed that this term is very small at infrared wavelengths], the upwelling all-sky radiative transfer equation for a given infrared channel or wavelength can be written as in Eq. (A3):

$$R_{obs}(\lambda) = [1 - \varepsilon(\lambda)][\varepsilon_{sfc}(\lambda)B(T_{sfc})T_{bc}(\lambda)T_{ac}(\lambda) + R_{bc}(\lambda)T_{ac}(\lambda)] + \varepsilon(\lambda)B(\lambda, T_{eff})T_{ac}(\lambda) + R_{ac}(\lambda). \quad \text{(A3)}$$

In Eq. (A3), R_{obs} is the observed radiance, $\varepsilon(\lambda)$ is the effective cloud emissivity, and T_{eff} is the effective cloud temperature. All other terms were previously defined. Equation (A2) can be used to rewrite Eq. (A3) as follows:

$$R_{obs}(\lambda) = [1 - \varepsilon(\lambda)][R_{clr}(\lambda) - R_{ac}(\lambda)] + \varepsilon(\lambda)B(\lambda, T_{eff})T_{ac}(\lambda) + R_{ac}(\lambda). \quad \text{(A4)}$$

Last, Eq. (A4) is algebraically reexpressed as shown in Eq. (A5) below:

$$R_{obs}(\lambda) = \varepsilon(\lambda)R_{ac}(\lambda) + T_{ac}(\lambda)\varepsilon(\lambda)B(\lambda, T_{eff}) + R_{clr}(\lambda)[1 - \varepsilon(\lambda)]. \quad \text{(A5)}$$

Eq. (A5) is the form of the all-sky form of the infrared radiative transfer equation that is used throughout this paper. This is the same form of the all-sky radiative transfer equation used in Heidinger and Pavolonis (2009).

APPENDIX B

Derivation of Analytical Expressions for the Jacobians Listed in Table 1

The infrared radiative transfer equation can be expressed as

$$R_{obs}(\lambda) = \varepsilon(\lambda)R_{ac}(\lambda) + T_{ac}(\lambda)\varepsilon(\lambda)B(\lambda, T_{eff}) + R_{clr}(\lambda)[1 - \varepsilon(\lambda)]. \quad \text{(B1)}$$

In the above equation, λ is wavelength, $R_{obs}(\lambda)$ is the observed radiance, $R_{clr}(\lambda)$ is the clear-sky radiance, $R_{ac}(\lambda)$ and $T_{ac}(\lambda)$ are the above-cloud upwelling atmospheric radiance and transmittance, respectively, B is the Planck function, T_{eff} is the effective cloud temperature, and ε is the cloud emissivity. In the infrared, the surface reflectance term is generally very small so that the clear-sky radiance $R_{clr}(\lambda)$ can be expressed as

$$R_{clr}(\lambda) = \varepsilon_{sfc}(\lambda)B(\lambda, T_{sfc})T_{atmos}(\lambda) + R_{atmos}(\lambda). \quad \text{(B2)}$$

In Eq. (B2), $\varepsilon_{sfc}(\lambda)$ is the surface emissivity, T_{sfc} is the surface temperature, $T_{atmos}(\lambda)$ is the surface-to-TOA transmittance, and $R_{atmos}(\lambda)$ is the integrated atmospheric radiance that is transmitted to the TOA, which can be approximated by Eq. (B3):

$$R_{atmos}(\lambda) \approx R_{atmos-1}(\lambda) + B(\lambda, T_{avg}) \times [T_{atmos-1}(\lambda) - T_{atmos}(\lambda)]. \quad \text{(B3)}$$

In Eq. (B3), $R_{atmos-1}(\lambda)$ is the integrated atmospheric radiance that excludes the lowest (e.g., near the surface) atmospheric layer, $B(\lambda, T_{avg})$ is the blackbody radiance based on the average temperature of the lowest atmospheric layer, and $T_{atmos-1}$ is the transmittance of the atmosphere excluding the lowest layer. This expression is needed when evaluating radiometric sensitivity to atmospheric transmittance.

Eq. (B1) can be rearranged and solved for cloud emissivity, as shown below:

$$\varepsilon(\lambda) = \frac{R_{obs}(\lambda) - R_{clr}(\lambda)}{R_{cld}(\lambda) - R_{clr}(\lambda)}. \quad \text{(B4)}$$

In (B4), a new variable R_{cld} is defined for notational convenience:

$$R_{cld}(\lambda) = R_{ac}(\lambda) + B(\lambda, T_{eff})T_{ac}(\lambda). \quad \text{(B5)}$$

In this sensitivity analysis, it is assumed that the effective cloud temperature T_{eff} is equal to the tropopause temperature T_{tropo}. As such, the effective absorption cloud optical depth ratio using the top-of-troposphere assumption, $\beta_{tropo}(\lambda_N, \lambda_D)$, is defined by

$$\beta_{\text{tropo}}(\lambda_N, \lambda_D) = \frac{\ln[1 - \varepsilon_{\text{tropo}}(\lambda_N)]}{\ln[1 - \varepsilon_{\text{tropo}}(\lambda_D)]}. \quad \text{(B6)}$$

The cloud emissivity calculated by assuming $T_{\text{eff}} = T_{\text{tropo}}$ is given by $\varepsilon_{\text{tropo}}$. In addition, λ_N and λ_D represent the wavelength used in the numerator and denominator of Eq. (B6), respectively. For the same given pair of wavelengths λ_N and λ_D, a BTD can be defined such that

$$\begin{aligned}\text{BTD}(\lambda_N, \lambda_D) &= \text{BT}(\lambda_D) - \text{BT}(\lambda_N) \\ &= B^{-1}[\lambda_D, R_{\text{obs}}(\lambda_D)] - B^{-1}[\lambda_N, R_{\text{obs}}(\lambda_N)].\end{aligned} \quad \text{(B7)}$$

In Eq. (B7), BT is the brightness temperature at a given wavelength, which is determined by applying the inverse of the Planck function (B^{-1}) to the radiance R_{obs}.

The spectral variation in the total clear-sky atmospheric transmittance $[\beta_{\text{atmos}}(\lambda_N, \lambda_D)]$ and surface emissivity $[\beta_{\text{sfc}}(\lambda_N, \lambda_D)]$ can be captured with expressions of the same form as the ratio of effective absorption cloud optical depth:

$$\beta_{\text{atmos}}(\lambda_N, \lambda_D) = \frac{\ln[T_{\text{atmos}}(\lambda_N)]}{\ln[T_{\text{atmos}}(\lambda_D)]} \quad \text{and} \quad \text{(B8)}$$

$$\beta_{\text{sfc}}(\lambda_N, \lambda_D) = \frac{\ln[1 - \varepsilon_{\text{sfc}}(\lambda_N)]}{\ln[1 - \varepsilon_{\text{sfc}}(\lambda_D)]}. \quad \text{(B9)}$$

We now define some common partial derivatives using Eqs. (B1)–(B9) [all of the symbols used in the following equations have been previously defined, with the exception of $\partial B(\lambda)/\partial T$, which is simply the derivative of the Planck function with respect to temperature]:

$$\frac{\partial \beta_{\text{tropo}}(\lambda_N, \lambda_D)}{\partial \varepsilon_{\text{tropo}}(\lambda_N)} = \frac{-1}{\ln[1.0 - \varepsilon_{\text{tropo}}(\lambda_D)][1 - \varepsilon_{\text{tropo}}(\lambda_N)]}, \quad \text{(B10)}$$

$$\frac{\partial \beta_{\text{tropo}}(\lambda_N, \lambda_D)}{\partial \varepsilon_{\text{tropo}}(\lambda_D)} = \frac{\ln[1.0 - \varepsilon_{\text{tropo}}(\lambda_N)]}{\ln[1.0 - \varepsilon_{\text{tropo}}(\lambda_D)]^2[1 - \varepsilon_{\text{tropo}}(\lambda_D)]}, \quad \text{(B11)}$$

$$\frac{\partial \varepsilon_{\text{tropo}}(\lambda_N)}{\partial R_{\text{obs}}(\lambda_N)} = \frac{\partial \varepsilon_{\text{tropo}}(\lambda_D)}{\partial R_{\text{obs}}(\lambda_D)} = \frac{1}{R_{\text{cld}}(\lambda) - R_{\text{clr}}(\lambda)}, \quad \text{(B12)}$$

$$\begin{aligned}\frac{\partial \varepsilon_{\text{tropo}}(\lambda_N)}{\partial R_{\text{clr}}(\lambda_N)} = \frac{\partial \varepsilon_{\text{tropo}}(\lambda_D)}{\partial R_{\text{clr}}(\lambda_D)} &= \frac{\varepsilon_{\text{cld}}(\lambda)[R_{\text{cld}}(\lambda) - R_{\text{clr}}(\lambda)]}{[R_{\text{cld\_tropo}}(\lambda) - R_{\text{clr}}(\lambda)]^2} \\ &\quad - \frac{\varepsilon_{\text{cld}}(\lambda)}{R_{\text{cld\_tropo}}(\lambda) - R_{\text{clr}}(\lambda)}\end{aligned} \quad \text{(B13)}$$

{in deriving Eq. (B13), it is important to remember to include the dependence of $R_{\text{obs}}(\lambda)$ on $R_{\text{clr}}(\lambda)$ [see Eqs. (B1) and (B4)]},

$$\begin{aligned}\frac{\partial R_{\text{obs}}(\lambda_N)}{\partial \beta(\lambda_N, \lambda_D)} &= \ln[1 - \varepsilon_{\text{cld}}(\lambda_D)][1 - \varepsilon_{\text{cld}}(\lambda_D)]^{\beta(\lambda_N, \lambda_D)} \\ &\quad \times [R_{\text{clr}}(\lambda_N) - R_{\text{cld}}(\lambda_N)],\end{aligned} \quad \text{(B14)}$$

$$\begin{aligned}\frac{\partial R_{\text{obs}}(\lambda_N)}{\partial \varepsilon_{\text{cld}}(\lambda_D)} &= \beta(\lambda_N, \lambda_D)[1 - \varepsilon_{\text{cld}}(\lambda_D)]^{[\beta(\lambda_N, \lambda_D) - 1]} \\ &\quad \times [R_{\text{cld}}(\lambda_N) - R_{\text{clr}}(\lambda_N)],\end{aligned} \quad \text{(B15)}$$

$$\frac{\partial R_{\text{obs}}(\lambda_D)}{\partial \varepsilon_{\text{cld}}(\lambda_D)} = R_{\text{cld}}(\lambda_D) - R_{\text{clr}}(\lambda_D), \quad \text{(B16)}$$

$$\frac{\partial R_{\text{obs}}(\lambda_N)}{\partial R_{\text{clr}}(\lambda_N)} = \frac{\partial R_{\text{obs}}(\lambda_D)}{\partial R_{\text{clr}}(\lambda_D)} = 1 - \varepsilon_{\text{cld}}(\lambda), \quad \text{(B17)}$$

$$\frac{\partial R_{\text{clr}}(\lambda_N)}{\partial T_{\text{sfc}}} = \frac{\partial R_{\text{clr}}(\lambda_D)}{\partial T_{\text{sfc}}} = \varepsilon_{\text{sfc}}(\lambda) T_{\text{atmos}}(\lambda) \left[\frac{\partial B(\lambda)}{\partial T_{\text{sfc}}}\right]^{-1}, \quad \text{(B18)}$$

$$\frac{\partial R_{\text{obs}}(\lambda_N)}{\partial T_{\text{eff}}} = \frac{\partial R_{\text{obs}}(\lambda_D)}{\partial T_{\text{eff}}} = \varepsilon_{\text{cld}}(\lambda) T_{\text{ac}}(\lambda) \left[\frac{\partial B(\lambda)}{\partial T_{\text{eff}}}\right]^{-1}, \quad \text{(B19)}$$

$$\begin{aligned}\frac{\partial R_{\text{clr}}(\lambda_N)}{\partial \varepsilon_{\text{sfc}}(\lambda_D)} &= \beta_{\text{sfc}}(\lambda_N, \lambda_D)[1 - \varepsilon_{\text{sfc}}(\lambda_D)]^{[\beta_{\text{sfc}}(\lambda_N, \lambda_D) - 1]} \\ &\quad \times T_{\text{atmos}}(\lambda_N) B(\lambda_N, T_{\text{sfc}}),\end{aligned} \quad \text{(B20)}$$

$$\frac{\partial R_{\text{clr}}(\lambda_D)}{\partial \varepsilon_{\text{sfc}}(\lambda_D)} = T_{\text{atmos}}(\lambda_D) B(\lambda_D, T_{\text{sfc}}), \quad \text{(B21)}$$

$$\begin{aligned}\frac{\partial R_{\text{clr}}(\lambda_N)}{\partial \beta_{\text{sfc}}(\lambda_N, \lambda_D)} &= -\ln[1 - \varepsilon_{\text{sfc}}(\lambda_D)][1 - \varepsilon_{\text{sfc}}(\lambda_D)]^{\beta_{\text{sfc}}(\lambda_N, \lambda_D)} \\ &\quad \times T_{\text{atmos}}(\lambda_N) B(\lambda_N, T_{\text{sfc}}),\end{aligned} \quad \text{(B22)}$$

$$\begin{aligned}\frac{\partial R_{\text{clr}}(\lambda_N)}{\partial T_{\text{atmos}}(\lambda_D)} &= \beta_{\text{atmos}}(\lambda_N, \lambda_D)[T_{\text{atmos}}(\lambda_D)]^{[\beta_{\text{atmos}}(\lambda_N, \lambda_D) - 1]} \\ &\quad \times [\varepsilon_{\text{sfc}}(\lambda_N) B(\lambda_N, T_{\text{sfc}}) - B(\lambda_N, T_{\text{avg}})],\end{aligned} \quad \text{(B23)}$$

$$\frac{\partial R_{\text{clr}}(\lambda_D)}{\partial T_{\text{atmos}}(\lambda_D)} = \varepsilon_{\text{sfc}}(\lambda_D) B(\lambda_D, T_{\text{sfc}}) - B(\lambda_D, T_{\text{avg}}), \quad \text{and} \quad \text{(B24)}$$

$$\begin{aligned}\frac{\partial R_{\text{clr}}(\lambda_N)}{\partial \beta_{\text{atmos}}(\lambda_N, \lambda_D)} &= \ln[T_{\text{atmos}}(\lambda_D)][T_{\text{atmos}}(\lambda_D)]^{\beta_{\text{atmos}}(\lambda_N, \lambda_D)} \\ &\quad \times [B(\lambda_N, T_{\text{sfc}}) - B(\lambda_N, T_{\text{avg}})].\end{aligned} \quad \text{(B25)}$$

Eqs. (B10)–(B25) are used to derive analytical expressions for all of the partial derivatives listed in Table 1 via application of the chain rule of calculus. For clarity, these expressions include the equation number of each previously defined derivative used, but be aware that the wavelength dependence is not shown in tandem with the equation number. There are derivatives with respect to cloud microphysics:

$$\frac{\partial \mathrm{BTD}(\lambda_N, \lambda_D)}{\partial \beta(\lambda_N, \lambda_D)} = -\frac{\partial R_{\mathrm{obs}}(\lambda_N)}{\partial \beta(\lambda_N, \lambda_D)}\left[\frac{\partial B(\lambda_N)}{\partial T}\right]^{-1} = -(\mathrm{B14})\left[\frac{\partial B(\lambda_N)}{\partial T}\right]^{-1} \tag{B26}$$

and

$$\frac{\partial \beta_{\mathrm{tropo}}(\lambda_N, \lambda_D)}{\partial \beta(\lambda_N, \lambda_D)} = \frac{\partial \beta_{\mathrm{tropo}}(\lambda_N, \lambda_D)}{\partial \varepsilon_{\mathrm{tropo}}(\lambda_N)}\frac{\partial \varepsilon_{\mathrm{tropo}}(\lambda_N)}{\partial R_{\mathrm{obs}}(\lambda_N)}\frac{\partial R_{\mathrm{obs}}(\lambda_N)}{\partial \beta(\lambda_N, \lambda_D)} = (\mathrm{B10})(\mathrm{B12})(\mathrm{B14}), \tag{B27}$$

derivatives with respect to the effective cloud temperature:

$$\frac{\partial \mathrm{BTD}(\lambda_N, \lambda_D)}{\partial T_{\mathrm{eff}}} = \frac{\partial R_{\mathrm{obs}}(\lambda_D)}{\partial T_{\mathrm{eff}}}\left[\frac{\partial B(\lambda_D)}{\partial T}\right]^{-1} - \frac{\partial R_{\mathrm{obs}}(\lambda_N)}{\partial T_{\mathrm{eff}}} \times \left[\frac{\partial B(\lambda_N)}{\partial T}\right]^{-1} = (\mathrm{B19})\left[\frac{\partial B(\lambda_D)}{\partial T}\right]^{-1} - (\mathrm{B19})\left[\frac{\partial B(\lambda_N)}{\partial T}\right]^{-1} \quad \text{and} \tag{B28}$$

$$\frac{\partial \beta_{\mathrm{tropo}}(\lambda_N, \lambda_D)}{\partial T_{\mathrm{eff}}} = \frac{\partial \beta_{\mathrm{tropo}}(\lambda_N, \lambda_D)}{\partial \varepsilon_{\mathrm{tropo}}(\lambda_N)}\frac{\partial \varepsilon_{\mathrm{tropo}}(\lambda_N)}{\partial R_{\mathrm{obs}}(\lambda_N)}\frac{\partial R_{\mathrm{obs}}(\lambda_N)}{\partial T_{\mathrm{eff}}} + \frac{\partial \beta_{\mathrm{tropo}}(\lambda_N, \lambda_D)}{\partial \varepsilon_{\mathrm{tropo}}(\lambda_D)}\frac{\partial \varepsilon_{\mathrm{tropo}}(\lambda_D)}{\partial R_{\mathrm{obs}}(\lambda_D)}\frac{\partial R_{\mathrm{obs}}(\lambda_D)}{\partial T_{\mathrm{eff}}} = (\mathrm{B10})(\mathrm{B12})(\mathrm{B19}) + (\mathrm{B11})(\mathrm{B12})(\mathrm{B19}), \tag{B29}$$

derivatives with respect to cloud emissivity:

$$\frac{\partial \mathrm{BTD}(\lambda_N, \lambda_D)}{\partial \varepsilon_{\mathrm{cld}}(\lambda_D)} = \frac{\partial R_{\mathrm{obs}}(\lambda_D)}{\partial \varepsilon_{\mathrm{cld}}(\lambda_D)}\left[\frac{\partial B(\lambda_D)}{\partial T}\right]^{-1} - \frac{\partial R_{\mathrm{obs}}(\lambda_N)}{\partial \varepsilon_{\mathrm{cld}}(\lambda_D)} \times \left[\frac{\partial B(\lambda_N)}{\partial T}\right]^{-1} = (\mathrm{B16})\left[\frac{\partial B(\lambda_D)}{\partial T}\right]^{-1} - (\mathrm{B15})\left[\frac{\partial B(\lambda_N)}{\partial T}\right]^{-1} \quad \text{and} \tag{B30}$$

$$\frac{\partial \beta_{\mathrm{tropo}}(\lambda_N, \lambda_D)}{\partial \varepsilon_{\mathrm{cld}}(\lambda_D)} = \frac{\partial \beta_{\mathrm{tropo}}(\lambda_N, \lambda_D)}{\partial \varepsilon_{\mathrm{tropo}}(\lambda_N)}\frac{\partial \varepsilon_{\mathrm{tropo}}(\lambda_N)}{\partial R_{\mathrm{obs}}(\lambda_N)}\frac{\partial R_{\mathrm{obs}}(\lambda_N)}{\partial \varepsilon_{\mathrm{cld}}(\lambda_D)} + \frac{\partial \beta_{\mathrm{tropo}}(\lambda_N, \lambda_D)}{\partial \varepsilon_{\mathrm{tropo}}(\lambda_D)}\frac{\partial \varepsilon_{\mathrm{tropo}}(\lambda_D)}{\partial R_{\mathrm{obs}}(\lambda_D)}\frac{\partial R_{\mathrm{obs}}(\lambda_D)}{\partial \varepsilon_{\mathrm{cld}}(\lambda_D)} = (\mathrm{B10})(\mathrm{B12})(\mathrm{B15}) + (\mathrm{B11})(\mathrm{B12})(\mathrm{B16}), \tag{B31}$$

derivatives with respect to surface temperature:

$$\frac{\partial \mathrm{BTD}(\lambda_N, \lambda_D)}{\partial T_{\mathrm{sfc}}} = \frac{\partial R_{\mathrm{obs}}(\lambda_D)}{\partial R_{\mathrm{clr}}(\lambda_D)}\frac{\partial R_{\mathrm{clr}}(\lambda_D)}{\partial T_{\mathrm{sfc}}}\left[\frac{\partial B(\lambda_D)}{\partial T}\right]^{-1} - \frac{\partial R_{\mathrm{obs}}(\lambda_N)}{\partial R_{\mathrm{clr}}(\lambda_N)}\frac{\partial R_{\mathrm{clr}}(\lambda_N)}{\partial T_{\mathrm{sfc}}}\left[\frac{\partial B(\lambda_N)}{\partial T}\right]^{-1} = (\mathrm{B17})(\mathrm{B18})\left[\frac{\partial B(\lambda_D)}{\partial T}\right]^{-1} - (\mathrm{B17})(\mathrm{B18})\left[\frac{\partial B(\lambda_N)}{\partial T}\right]^{-1} \quad \text{and} \tag{B32}$$

$$\frac{\partial \beta_{\mathrm{tropo}}(\lambda_N, \lambda_D)}{\partial T_{\mathrm{sfc}}} = \frac{\partial \beta_{\mathrm{tropo}}(\lambda_N, \lambda_D)}{\partial \varepsilon_{\mathrm{tropo}}(\lambda_N)}\frac{\partial \varepsilon_{\mathrm{tropo}}(\lambda_N)}{\partial R_{\mathrm{clr}}(\lambda_N)}\frac{\partial R_{\mathrm{clr}}(\lambda_N)}{\partial T_{\mathrm{sfc}}} + \frac{\partial \beta_{\mathrm{tropo}}(\lambda_N, \lambda_D)}{\partial \varepsilon_{\mathrm{tropo}}(\lambda_D)}\frac{\partial \varepsilon_{\mathrm{tropo}}(\lambda_D)}{\partial R_{\mathrm{clr}}(\lambda_D)}\frac{\partial R_{\mathrm{clr}}(\lambda_D)}{\partial T_{\mathrm{sfc}}} = (\mathrm{B10})(\mathrm{B13})(\mathrm{B18}) + (\mathrm{B11})(\mathrm{B13})(\mathrm{B18}), \tag{B33}$$

derivatives with respect to the denominator clear-sky transmittance:

$$\frac{\partial \mathrm{BTD}(\lambda_N, \lambda_D)}{\partial T_{\mathrm{atmos}}(\lambda_D)} = \frac{\partial R_{\mathrm{obs}}(\lambda_D)}{\partial R_{\mathrm{clr}}(\lambda_D)}\frac{\partial R_{\mathrm{clr}}(\lambda_D)}{\partial T_{\mathrm{atmos}}(\lambda_D)}\left[\frac{\partial B(\lambda_D)}{\partial T}\right]^{-1} - \frac{\partial R_{\mathrm{obs}}(\lambda_N)}{\partial R_{\mathrm{clr}}(\lambda_N)}\frac{\partial R_{\mathrm{clr}}(\lambda_N)}{\partial T_{\mathrm{atmos}}(\lambda_D)}\left[\frac{\partial B(\lambda_N)}{\partial T}\right]^{-1} = (\mathrm{B17})(\mathrm{B24})\left[\frac{\partial B(\lambda_D)}{\partial T}\right]^{-1} - (\mathrm{B17})(\mathrm{B23})\left[\frac{\partial B(\lambda_N)}{\partial T}\right]^{-1} \quad \text{and} \tag{B34}$$

$$\frac{\partial \beta_{\mathrm{tropo}}(\lambda_N, \lambda_D)}{\partial T_{\mathrm{atmos}}(\lambda_D)} = \frac{\partial \beta_{\mathrm{tropo}}(\lambda_N, \lambda_D)}{\partial \varepsilon_{\mathrm{tropo}}(\lambda_N)}\frac{\partial \varepsilon_{\mathrm{tropo}}(\lambda_N)}{\partial R_{\mathrm{clr}}(\lambda_N)}\frac{\partial R_{\mathrm{clr}}(\lambda_N)}{\partial T_{\mathrm{atmos}}(\lambda_D)} + \frac{\partial \beta_{\mathrm{tropo}}(\lambda_N, \lambda_D)}{\partial \varepsilon_{\mathrm{tropo}}(\lambda_D)}\frac{\partial \varepsilon_{\mathrm{tropo}}(\lambda_D)}{\partial R_{\mathrm{clr}}(\lambda_D)}\frac{\partial R_{\mathrm{clr}}(\lambda_D)}{\partial T_{\mathrm{atmos}}(\lambda_D)} = (\mathrm{B10})(\mathrm{B13})(\mathrm{B23}) + (\mathrm{B11})(\mathrm{B13})(\mathrm{B24}), \tag{B35}$$

derivatives with respect to the spectral variation of clear-sky transmittance:

$$\frac{\partial \mathrm{BTD}(\lambda_N,\lambda_D)}{\partial \beta_{\mathrm{atmos}}(\lambda_N,\lambda_D)} = -\frac{\partial R_{\mathrm{obs}}(\lambda_N)}{\partial R_{\mathrm{clr}}(\lambda_N)}\frac{\partial R_{\mathrm{clr}}(\lambda_N)}{\partial \beta_{\mathrm{atmos}}(\lambda_N,\lambda_D)}\left[\frac{\partial B(\lambda_N)}{\partial T}\right]^{-1} = -(\mathrm{B17})(\mathrm{B25})\left[\frac{\partial B(\lambda_N)}{\partial T}\right]^{-1} \quad \text{and} \tag{B36}$$

$$\frac{\partial \beta_{\mathrm{tropo}}(\lambda_N,\lambda_D)}{\partial \beta_{\mathrm{atmos}}(\lambda_N,\lambda_D)} = \frac{\partial \beta_{\mathrm{tropo}}(\lambda_N,\lambda_D)}{\partial \varepsilon_{\mathrm{tropo}}(\lambda_N)}\frac{\partial \varepsilon_{\mathrm{tropo}}(\lambda_N)}{\partial R_{\mathrm{clr}}(\lambda_N)} \times \frac{\partial R_{\mathrm{clr}}(\lambda_N)}{\partial \beta_{\mathrm{atmos}}(\lambda_N,\lambda_D)} = (\mathrm{B10})(\mathrm{B13})(\mathrm{B25}), \tag{B37}$$

derivatives with respect to the denominator surface emissivity:

$$\frac{\partial \mathrm{BTD}(\lambda_N,\lambda_D)}{\partial \varepsilon_{\mathrm{sfc}}(\lambda_D)} = \frac{\partial R_{\mathrm{obs}}(\lambda_D)}{\partial R_{\mathrm{clr}}(\lambda_D)}\frac{\partial R_{\mathrm{clr}}(\lambda_D)}{\partial \varepsilon_{\mathrm{sfc}}(\lambda_D)}\left[\frac{\partial B(\lambda_D)}{\partial T}\right]^{-1} - \frac{\partial R_{\mathrm{obs}}(\lambda_N)}{\partial R_{\mathrm{clr}}(\lambda_N)}\frac{\partial R_{\mathrm{clr}}(\lambda_N)}{\partial \varepsilon_{\mathrm{sfc}}(\lambda_D)}\left[\frac{\partial B(\lambda_N)}{\partial T}\right]^{-1} = (\mathrm{B17})(\mathrm{B21})\left[\frac{\partial B(\lambda_D)}{\partial T}\right]^{-1} - (\mathrm{B17})(\mathrm{B20})\left[\frac{\partial B(\lambda_N)}{\partial T}\right]^{-1} \quad \text{and} \tag{B38}$$

$$\frac{\partial \beta_{\mathrm{tropo}}(\lambda_N,\lambda_D)}{\partial \varepsilon_{\mathrm{sfc}}(\lambda_D)} = \frac{\partial \beta_{\mathrm{tropo}}(\lambda_N,\lambda_D)}{\partial \varepsilon_{\mathrm{tropo}}(\lambda_N)}\frac{\partial \varepsilon_{\mathrm{tropo}}(\lambda_N)}{\partial R_{\mathrm{clr}}(\lambda_N)}\frac{\partial R_{\mathrm{clr}}(\lambda_N)}{\partial \varepsilon_{\mathrm{sfc}}(\lambda_D)} + \frac{\partial \beta_{\mathrm{tropo}}(\lambda_N,\lambda_D)}{\partial \varepsilon_{\mathrm{tropo}}(\lambda_D)}\frac{\partial \varepsilon_{\mathrm{tropo}}(\lambda_D)}{\partial R_{\mathrm{clr}}(\lambda_D)}\frac{\partial R_{\mathrm{clr}}(\lambda_D)}{\partial \varepsilon_{\mathrm{sfc}}(\lambda_D)} = (\mathrm{B10})(\mathrm{B13})(\mathrm{B20}) + (\mathrm{B11})(\mathrm{B13})(\mathrm{B21}), \tag{B39}$$

and derivatives with respect to the spectral variation of surface emissivity:

$$\frac{\partial \mathrm{BTD}(\lambda_N,\lambda_D)}{\partial \beta_{\mathrm{sfc}}(\lambda_N,\lambda_D)} = -\frac{\partial R_{\mathrm{obs}}(\lambda_N)}{\partial R_{\mathrm{clr}}(\lambda_N)}\frac{\partial R_{\mathrm{clr}}(\lambda_N)}{\partial \beta_{\mathrm{sfc}}(\lambda_N,\lambda_D)}\left[\frac{\partial B(\lambda_N)}{\partial T}\right]^{-1} = -(\mathrm{B17})(\mathrm{B22})\left[\frac{\partial B(\lambda_N)}{\partial T}\right]^{-1} \quad \text{and} \tag{B40}$$

$$\frac{\partial \beta_{\mathrm{tropo}}(\lambda_N,\lambda_D)}{\partial \beta_{\mathrm{sfc}}(\lambda_N,\lambda_D)} = \frac{\partial \beta_{\mathrm{tropo}}(\lambda_N,\lambda_D)}{\partial \varepsilon_{\mathrm{tropo}}(\lambda_N)}\frac{\partial \varepsilon_{\mathrm{tropo}}(\lambda_N)}{\partial R_{\mathrm{clr}}(\lambda_N)}\frac{\partial R_{\mathrm{clr}}(\lambda_N)}{\partial \beta_{\mathrm{sfc}}(\lambda_N,\lambda_D)} = (\mathrm{B10})(\mathrm{B13})(\mathrm{B22}). \tag{B41}$$

Last, all of these partial derivatives are evaluated under various assumed conditions. The magnitude of each (after proper scaling, since the units differ) can be used to assess the sensitivity of $\beta_{\mathrm{tropo}}(\lambda_N,\lambda_D)$ and $\mathrm{BTD}(\lambda_N,\lambda_D)$ to local changes in the various dependent variables.

REFERENCES

Adler, R. F., and D. D. Fenn, 1979: Thunderstorm intensity as determined from satellite data. *J. Appl. Meteor.,* **18,** 502–517.

Baum, B. A., P. F. Soulen, K. I. Strabala, M. D. King, S. A. Ackerman, W. P. Menzel, and P. Yang, 2000: Remote sensing of cloud properties using MODIS airborne simulator imagery during SUCCESS 2. Cloud thermodynamic phase. *J. Geophys. Res.,* **105,** 11 781–11 792.

Clough, S. A., and M. J. Iacono, 1995: Line-by-line calculation of atmospheric fluxes and cooling rates 2. Application to carbon dioxide, ozone, methane, nitrous oxide and the halocarbons. *J. Geophys. Res.,* **100,** 16 519–16 535.

Cox, S. K., 1976: Observations of cloud infrared effective emissivity. *J. Atmos. Sci.,* **33,** 287–289.

Downing, H. D., and D. Williams, 1975: Optical constants of water in infrared. *J. Geophys. Res.,* **80,** 1656–1661.

Dunion, J. P., and C. S. Velden, 2004: The impact of the Saharan air layer on Atlantic tropical cyclone activity. *Bull. Amer. Meteor. Soc.,* **85,** 353–365.

Evan, A. T., D. J. Vimont, A. K. Heidinger, J. P. Kossin, and R. Bennartz, 2009: The role of aerosols in the evolution of tropical North Atlantic Ocean temperature anomalies. *Science,* **324,** 778–781, doi:10.1126/science.1167404.

Giraud, V., J. C. Buriez, Y. Fouquart, F. Parol, and G. Seze, 1997: Large-scale analysis of cirrus clouds from AVHRR data: Assessment of both a microphysical index and the cloud-top temperature. *J. Appl. Meteor.,* **36,** 664–675.

Hamill, T. M., J. S. Whitaker, and S. L. Mullen, 2006: Reforecasts: An important dataset for improving weather predictions. *Bull. Amer. Meteor. Soc.,* **87,** 33–46.

Hannon, S., L. L. Strow, and W. W. McMillan, 1996: Atmospheric infrared fast transmittance models: A comparison of two approaches. *Proc. Optical Spectroscopic Techniques and Instrumentation for Atmospheric and Space Research II,* P. B. Hays and J. Wang, Eds., International Society for Optical Engineering (SPIE Proceedings, Vol. 2830), 94–105.

Hansen, J. E., and L. D. Travis, 1974: Light scattering in planetary atmospheres. *Space Sci. Rev.,* **16,** 527–610.

Heidinger, A. K., and M. J. Pavolonis, 2009: Gazing at cirrus clouds for 25 years through a split window. Part I: Methodology. *J. Appl. Meteor. Climatol.,* **48,** 1110–1116.

Inoue, T., 1985: On the temperature and effective emissivity determination of semi-transparent cirrus clouds by bi-spectral measurements in the 10 μm window region. *J. Meteor. Soc. Japan,* **63,** 88–99.

——, 1987: A cloud type classification with *NOAA 7* split-window measurements. *J. Geophys. Res.,* **92** (D4), 3991–4000.

Lopez, M. A., D. L. Hartmann, P. N. Blossey, R. Wood, C. S. Bretherton, and T. L. Kubar, 2009: A test of the simulation of tropical convective cloudiness by a cloud resolving model. *J. Climate,* **22,** 2834–2849.

Mecikalski, J. R., and K. M. Bedka, 2006: Forecasting convective initiation by monitoring the evolution of moving cumulus in daytime GOES imagery. *Mon. Wea. Rev.,* **134,** 49–78.

Menzel, W. P., and Coauthors, 2008: MODIS global cloud-top pressure and amount estimation: Algorithm description and results. *J. Appl. Meteor. Climatol.,* **47,** 1175–1198.

Miller, T. P., and T. J. Casadevall, 2000: Volcanic ash hazards to aviation. *Encyclopedia of Volcanoes,* H. Sigurdsson, Ed., Academic Press, 915–930.

Minnis, P., D. F. Young, D. P. Garber, L. Nguyen, W. L. Smith, and R. Palikonda, 1998: Transformation of contrails into cirrus during SUCCESS. *Geophys. Res. Lett.,* **25,** 1157–1160.

——, J. K. Ayers, R. Palikonda, and D. Phan, 2004: Contrails, cirrus trends, and climate. *J. Climate,* **17,** 1671–1685.

Mitchell, D. L., 2000: Parameterization of the Mie extinction and absorption coefficients for water clouds. *J. Atmos. Sci.,* **57,** 1311–1326.

Nakajima, T., and M. D. King, 1990: Determination of the optical thickness and effective particle radius of clouds from reflected solar radiation measurements. Part I: Theory. *J. Atmos. Sci.,* **47,** 1878–1893.

Olander, T. L., and C. S. Velden, 2007: The advanced Dvorak technique: Continued development of an objective scheme to estimate tropical cyclone intensity using geostationary infrared satellite imagery. *Wea. Forecasting,* **22,** 287–298.

Parol, F., J. C. Buriez, G. Brogniez, and Y. Fouquart, 1991: Information content of AVHRR channels 4 and 5 with respect to the effective radius of cirrus cloud particles. *J. Appl. Meteor.,* **30,** 973–984.

Pavolonis, M. J., and A. K. Heidinger, 2004: Daytime cloud overlap detection from AVHRR and VIIRS. *J. Appl. Meteor.,* **43,** 762–778.

——, ——, and T. Uttal, 2005: Daytime global cloud typing from AVHRR and VIIRS: Algorithm description, validation, and comparisons. *J. Appl. Meteor.,* **44,** 804–826.

——, W. F. Feltz, A. K. Heidinger, and G. M. Gallina, 2006: A daytime complement to the reverse absorption technique for improved automated detection of volcanic ash. *J. Atmos. Oceanic Technol.,* **23,** 1422–1444.

Pollack, J. B., O. B. Toon, and B. N. Khare, 1973: Optical properties of some terrestrial rocks and glasses. *Icarus,* **19,** 372–389.

Prata, A. J., 1989: Observations of volcanic ash clouds in the 10-12-micron window using AVHRR/2 data. *Int. J. Remote Sens.,* **10,** 751–761.

Roush, T., J. Pollack, and J. Orenberg, 1991: Derivation of mid-infrared (5-25 μm) optical constants of some silicates and palagonite. *Icarus,* **94,** 191–208.

Seemann, S. W., E. E. Borbas, R. O. Knuteson, G. R. Stephenson, and H. Huang, 2008: Development of a global infrared land surface emissivity database for application to clear sky sounding retrievals from multispectral satellite radiance measurements. *J. Appl. Meteor. Climatol.,* **47,** 108–123.

Stamnes, K., S. C. Tsay, W. Wiscombe, and K. Jayaweera, 1988: Numerically stable algorithm for discrete-ordinate-method radiative transfer in multiple scattering and emitting layered media. *Appl. Opt.,* **27,** 2502–2509.

Strabala, K. I., S. A. Ackerman, and W. P. Menzel, 1994: Cloud properties inferred from 8–12-μm data. *J. Appl. Meteor.,* **33,** 212–229.

Strow, L. L., S. E. Hannon, S. De Souza-Machado, H. E. Motteler, and D. Tobin, 2003: An overview of the AIRS radiative transfer model. *IEEE Trans. Geosci. Remote Sens.,* **41,** 303–313, doi:10.1109/TGRS.2002.808244.

Turner, D. D., 2005: Arctic mixed-phase cloud properties from AERI lidar observations: Algorithm and results from SHEBA. *J. Appl. Meteor.,* **44,** 427–444.

Van de Hulst, H. C., 1980: *Multiple Light Scattering, Tables, Formulas, and Applications*. Vol. 2. Academic Press, 739 pp.

Warren, S. G., and R. E. Brandt, 2008: Optical constants of ice from the ultraviolet to the microwave: A revised compilation. *J. Geophys. Res.,* **113,** 14220, doi:10.1029/2007JD009744.

Yang, P., H. L. Wei, H. L. Huang, B. A. Baum, Y. X. Hu, G. W. Kattawar, M. I. Mishchenko, and Q. Fu, 2005: Scattering and absorption property database for nonspherical ice particles in the near- through far-infrared spectral region. *Appl. Opt.,* **44,** 5512–5523.

Zhang, H., and W. P. Menzel, 2002: Improvement in thin cirrus retrievals using an emissivity-adjusted CO_2 slicing algorithm. *J. Geophys. Res.,* **107,** 4327, doi:10.1029/2001JD001037.

Zhang, P., N. Lu, X. Hu, and C. Dong, 2006: Identification and physical retrieval of dust storm using three MODIS thermal IR channels. *Global Planet. Change,* **52,** 197–206, doi:10.1016/j.gloplacha.2006.02.014.